

## Research Paper

# Coupled aerothermal-mechanical analysis in single crystal double wall transpiration cooled gas turbine blades with a large film hole density

Matthew Courtis<sup>1</sup>, Christos Skamniotis<sup>1,\*</sup>, Alan Cocks, Peter Ireland<sup>\*</sup>

Department of Engineering Science, University of Oxford, OX2 OES, UK

## ARTICLE INFO

## Keywords:

Double wall transpiration cooling  
Gas turbine blades  
Gas ingestion  
Thermomechanical stresses  
Single crystal orientation  
Nickel superalloys

## ABSTRACT

The ambition for increasing gas turbine efficiency beyond current levels through the elevation of gas temperatures demands substantial progress in turbine blade cooling technology. Double wall transpiration cooling (DWTC) is an emerging technology which offers enhanced thermal protection at only modest coolant flows, thanks to a combination of impingement jets and densely packed arrays of film cooling holes. This paper presents a coupled aerothermal-mechanical investigation of a transpiration cooled double wall turbine blade design, by employing Computational Fluid Dynamics (CFD), heat transfer theory as well as stress analysis based on plate theory and Finite Element (FE) analysis. In comparison to previously explored systems with modest outer wall porosity, a system with high porosity is found to display enhanced cooling effectiveness and to reduce the temperature difference across the two walls that drives thermal stresses. This difference can be decreased further by reducing the wall spacing,  $H$ , or the inner-outer wall thickness ratio,  $t_c/t_h$ , at the cost of higher overall metal temperatures. A lower bound for  $H$  should be used to avoid undesirable poor coolant flow distribution and hot gas ingestion effects, whereas the  $t_c/t_h$  ratio does not impose any aerothermal constraints. Thermal stresses associated with a fixed temperature field are invariant with  $H$  but they vary drastically with  $t_c/t_h$ . From a design perspective, the above suggest that  $H$  is primarily determined by aerothermal requirements, whereas  $t_c/t_h$  by the mechanical performance. The single crystal orientation and elastic anisotropy of Nickel alloys are shown to have a profound impact on the stress concentration around cooling holes, with secondary crystallographic directions, such as  $\langle 110 \rangle$  and  $\langle 111 \rangle$ , playing a prominent role in the local stress state. Our study provides a framework for optimising the aerothermal and mechanical performance in a range of high temperature components and highlights key areas where more elaborate analysis is needed.

## 1. Introduction

Gas turbine efficiency depends on the level of thermomechanical loading that can be withstood by critical hot stage components, such as high-pressure turbine blades [5]. To address the increasing efficiency demands and environmental concerns, future cooling systems must continue to protect these components against even more aggressive heat fluxes, by using the minimum possible coolant mass flow [6]. To achieve this, effusion and transpiration type systems [7,8] with arrays of film cooling holes are being considered, which offer the benefits of higher internal surface area and elevated external film protection [9,10]. Recently, the double wall transpiration cooling (DWTC) system has been proposed to enhance the cooling capability through a combination of film and impingement cooling [11].

The repeating unit of one such system is depicted in Fig. 1d with a high outer wall porosity of 19.2 % associated with inclined film holes through which the coolant escapes to protect the metal against the external heat flux (Fig. 1e); prior to this, the coolant is impinged on the interior of the outer wall with the aid of transverse holes in an inner wall. The wall-connecting pedestals resist bursting loads and facilitate thermal conduction between the hotter outer wall and cooler inner wall. The outstanding cooling effectiveness of DWTC systems has been demonstrated through Computational Fluid Dynamics (CFD) analysis and empirical correlations by a number of authors, including Li et al. [11], Murray et al. [1] and Ngetich et al. [12]. The beneficial effect of film hole density, i.e. outer wall porosity, on film effectiveness has been demonstrated by Murray et al. [6] as well as Courtis et al. [9], who varied film hole spacing on a flat plate in a re-circulatory experimental facility, with results indicating that low film hole spacing increases

\* Corresponding authors.

E-mail addresses: [c.skamniotis@le.ac.uk](mailto:c.skamniotis@le.ac.uk) (C. Skamniotis), [peter.ireland@eng.ox.ac.uk](mailto:peter.ireland@eng.ox.ac.uk) (P. Ireland).

<sup>1</sup> Contributed equally.

<b>Nomenclature</b>		$B$	bulk Modulus (MPa)
<b>Abbreviations</b>		$\bar{E}$	volume averaged (isotropic) Young's modulus (MPa)
DWTC	double wall transpiration cooling	$\bar{\nu}$	volume averaged (isotropic) Poisson's ratio (-/-)
FE	Finite elements	$\bar{G}_{Hills}$	volume averaged (isotropic) shear modulus by Hill (MPa)
2D	two-dimensional	$E_R$	reference Young's modulus (MPa)
3D	three-dimensional	$\nu_R$	reference Poisson's ratio (-/-)
SCF	stress concentration factor	$C_{11}, C_{12}, C_{44}$	independent elastic constants for FCC crystal (MPa)
LCF	low cycle fatigue	$C, S$	elastic stiffness and compliance matrices for FCC crystal (MPa)
FCC	face centred cubic	$\hat{S}$	compliance matrix in the global coordinate system (MPa)
CFD	Computational fluid dynamics	$A$	Zener factor of anisotropy (-/-)
<b>Symbols Thermal</b>		$a$	thermal expansion coefficient (1/°C)
$T_{max}$	maximum temperature in the structure / temperature at the outer hot wall surface (°C)	[001], [010], [100]	principal crystallographic directions
$T_{med}$	temperature at the inner hot wall surface (°C)	{100}	family of principal crystallographic directions
$T_{min}$	minimum temperature in the structure / cool wall temperature (°C)	$\langle 100 \rangle$	family of compliant directions (cube normals)
$T_{\infty}$	external free-stream temperature (°C)	$\langle 110 \rangle$	family of medium stiffness directions (cube face diagonals)
$T_c$	coolant entry temperature (°C)	$\langle 111 \rangle$	family of stiff directions (cube diagonals)
$T_w, T_{aw}$	wall and adiabatic wall temperature (°C)	$\tau_{crss}$	critical resolved shear stress (MPa)
$T_{f,outlet}$	film hole outlet temperature (°C)	$\Delta \tau_{crss}$	sum of $\tau_{crss}$ at peak temperature and $\tau_{crss}$ at room temperature at a particular location in the system (MPa)
$T_0$	room temperature (°C)	<b>Mechanical</b>	
$\Delta T$	total temperature difference $T_{max} - T_{min}$ across the double walls/in the structure (°C)	$P_{CF}$	nominal centrifugal stress carried by walls (MPa)
$T(y)$	temperature as a function of though thickness position in the hot wall (°C)	$P_{CF,netMax}$	maximum net centrifugal stress carried by walls (MPa)
$\nu_f, \nu_{\infty}$	film jet and external flow velocity (m/s)	$\sigma_T$	reference thermal stress (MPa)
$\rho_f, \rho_{\infty}$	film jet and external flow density (kg/m <sup>3</sup> )	$S_h^M x, S_h^M z$	nominal membrane thermal stress in the hot wall along x, z
$\dot{m}_c$	mass flow rate (kg/m <sup>2</sup> /s)	$S_h^B x, S_h^B z$	nominal bending thermal stress in the hot wall along x, z
$m^*$	non-dimensional mass flow rate	$\sigma_{hx}, \sigma_{hz}$	nominal total stress in the hot wall along x, z
$M$	blowing ratio	$S_{cx}, S_{cz}$	nominal membrane thermal stress in the cool wall along the x and z directions
$\eta_f$	film effectiveness	$\sigma_{cx}, \sigma_{cz}$	nominal total stress in the cool wall along x, z
$\epsilon$	cooling effectiveness	$\sigma$	Cauchy stress tensor in the crystal system (MPa)
$Nu$	Nusselt number	$\sigma_1, \sigma_2, \sigma_3$	maximum, medium and minimum principal stresses (MPa)
$Re$	Reynolds number	$\tau_{rss}$	resolved shear stress in a particular crystallographic slip plane and direction (MPa)
$TF$	Transpiration factor ( $T_w - T_{f,outlet}$ difference divided by $T_{\infty} - T_c$ difference)	$\tau_{rss}$	12 × 1 column vector of resolved shear stresses in the 12 octahedral FCC slip systems (MPa)
<b>Structural</b>		SCF	stress concentration factor (MPa)
$t_h, t_c$	hot wall and cool wall thicknesses (mm)	$\omega$	turbine rotational speed (rpm)
$R$	geometric radius of curvature (mm)	<b>Spatial</b>	
$H$	wall spacing/pedestal height (mm)	XYZ	global coordinate system in turbine blade (mm)
$s$	unit cell length along x axis (mm)	xyz	local coordinate system in blade / global coordinate system in unit cell (mm)
$w$	unit cell width / pedestal centre line distance along z axis (mm)	$\xi$	circumferential/chord direction in turbine blade (mm)
$S$	gross wall cross sectional area (mm)	$Z, z$	axial direction in turbine blade (mm)
$D_{ped}$	pedestal square edge length (mm)	$\varphi, \hat{l}, \psi$	Euler angles defining the intrinsic FCC crystal rotation with respect to XYZ
$D_{film}, D_{imp}$	film hole and impingement hole diameters (mm)	$y$	position through hot wall thickness (mm)
$\gamma$	film hole angle (°)	$T$	3 × 3 transformation matrix between crystal system and global system
$\rho_{ped}, \rho_{hole}$	fillet radius for pedestal and holes (mm)	$\bar{T}$	equivalent 6 × 6 transformation matrix for column vector operations
$L$	blade length (mm)	$l_1, l_2, l_3$	direction cosines between crystal axes and global axe
$R_{tip}$	distance between the blade tip and the engine axis (mm)		
<b>Material</b>			
$\rho$	metal density (tn/mm3)		

mean film effectiveness, provides more uniform protection and reduces hot streaks. Wambersie et al. [13] explored the impact of high porosity panels on the suction and pressure surfaces of a turbine blade; a high film effectiveness was achieved with low mass flow rates, especially on the suction surface. Despite the wealth of recent studies on DWTCs, full thermal solutions for outer wall porosities as high as 20 % have not been

obtained. One of the key objectives of this study is to generate relevant solutions.

The relationship between the film hole density and the structural integrity of DWTCs has received even less attention. Relevant work has only been presented by the authors in terms of elastic theoretical and Finite Element (FE) analysis [2] and studies which consider local

inelastic deformation [14] in systems of relatively low outer wall porosity, of the order of 10 %. The repeating unit of one such system is shown in Fig. 2a2 and can be visually compared against the one studied here in Fig. 2a1. It was shown that since the walls are connected by rigid pedestals and experience different temperatures, they must extend equally in plane, causing membrane thermal stresses [15]. Additionally, a thermal gradient exists across the hot wall thickness but the wall rotations are self-constrained by the blade geometry, superimposing bending thermal stresses in the outer hot wall [15]. Mechanical stresses associated with centrifugal loading are also superimposed on the thermal stress field [2,16]. Locally, at holes and pedestals the stresses are magnified beyond yield, leading to reversed plastic straining and eventually localised cracking due to low cycle fatigue (LCF) [14]. Such inelastic effects were shown to be critical at external features, i.e. film holes, where the metal experiences its peak temperature and therefore can exhibit high creep rates and low yield strength [14]. It was suggested that geometric features should be modified towards minimising film hole stresses: by tailoring the film hole characteristics (inclination, ellipticity) to attenuate stress concentration effects, and simultaneously reducing the inner wall thickness to reduce the nominal thermal stresses in the outer wall [14].

None of these design recommendations have taken into account the role of material anisotropy. Moreover, no study reports on the effect of

internal features, i.e. inner to outer wall thickness ratio and wall spacing/pedestal height, on the cooling performance and resulting temperature field. These knowledge gaps highlight the need for a more comprehensive investigation of the aerothermal performance and stress fields, particularly when the design concerns highly porous single crystal turbine blade components. This need is addressed in the present paper through a combination of aerothermal and mechanical analyses via theoretical and numerical means. In particular, the following questions will be addressed:

- (1) what are the implications of using a high outer wall porosity on the aerothermal and mechanical performance?
- (2) how does the wall spacing/pedestal height and the inner wall thickness influence the aerothermal performance and temperature field?
- (3) how does anisotropy and crystal orientation influence nominal wall stresses and stress concentrations at features?
- (4) does a thinner cool wall result in a better overall mechanical performance in both isotropic and anisotropic systems?

We will consider the thermoelastic properties of the CMSX-4 Nickel superalloy, which is used extensively in gas turbine blades. Nevertheless, the theoretical-FE solutions and resulting phenomena presented

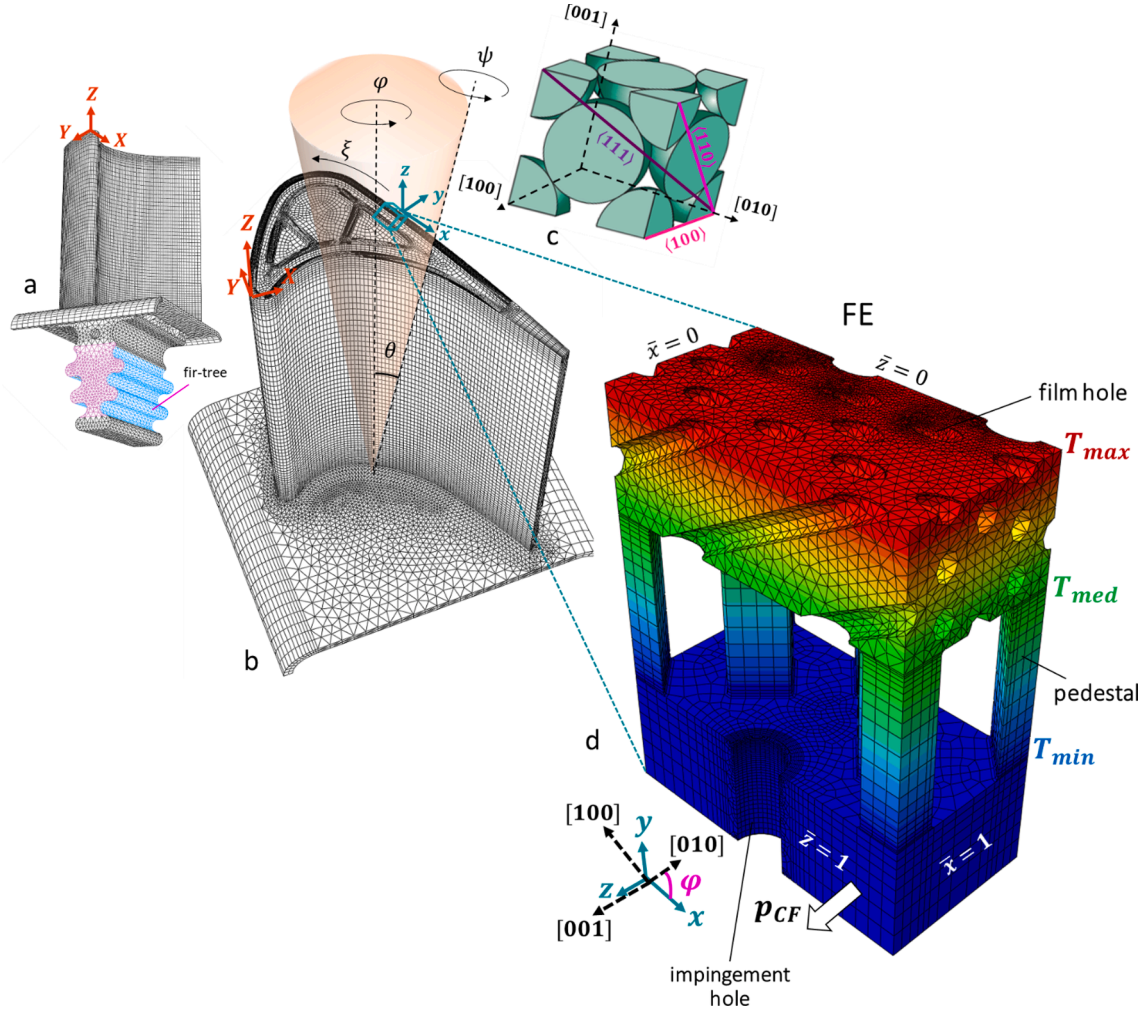


**Fig. 1.** (a-b) Double wall turbine blade FE model reproduced from [2];  $4 \times 10^5$  8-node hexahedral elements (ABAQUS code: C3D8T) are used to mesh the walls (25 elements across the wall thicknesses) and  $10^5$  4-node tetrahedral elements (C3D4T) are used to mesh the platform and fir-tree regions. (c) FCC crystal rotated by Euler angles  $\varphi$ ,  $\theta$ ,  $\psi$  in Fig. 3b with respect to the global blade system XYZ. (d) Flat unit cell with discrete pedestals and holes, corresponding to the low curvature region in Fig. 3b and the local blade system xyz; contours show the idealised temperature field;  $3 \times 10^4$  C3D8T elements are used to mesh the inner wall and pedestals and  $10^5$  C3D4T are used in the hot wall.

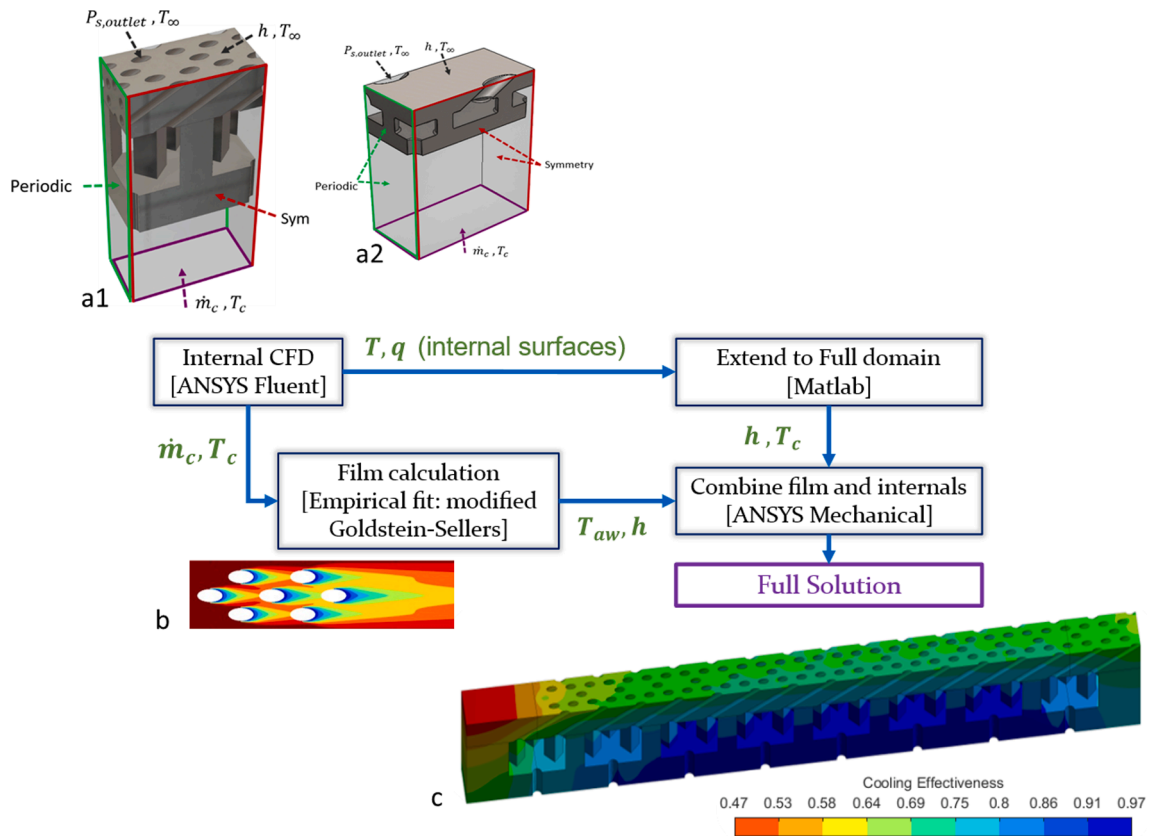


**Fig. 2.** Schematic of the conjugate aerothermal analysis method developed by Murray et al [1]. (a1) CFD model used in present study, corresponding to the repeating unit cell of the DWTC system with high outer wall porosity of 19.2 %. (a2) CFD model used previously in [2] for a DWTC system with low outer wall porosity of 10 %. (b) Illustration of cooling effectiveness calculated by the modified Goldstein-Sellers method. (c) Temperature field of the full streamwise domain for a non-dimensional coolant flow rate,  $m^* = 3$ , and the typical geometric ratios of  $t_c/D_{imp} = 2.86$  and  $H/D_{imp} = 4.29$ .

here are relevant to any cubic metal. These findings will provide a stepping-stone to performing LCF life calculations in single crystal DWTC systems, either through the development of an extended Neuber type scheme for anisotropic materials [17], and/or by the use of crystal plasticity Finite Element (CPFE) analysis [18]. The importance of an initial determination of peak stresses in the elastic regime has been demonstrated in [14].

The aerothermal analysis is conducted first in Section 2 with the objective of addressing question 3 above; the link between this analysis and the mechanical analysis is then discussed in Section 3, after which the mechanical analysis is performed, with questions 1 and 2 addressed in Section 4. An overall evaluation of our results and concluding remarks are provided in Sections 5 and 6.

## 2. Aerothermal analysis

### 2.1. Aerothermal model

We consider a low curvature (and low pressure) region of a double wall turbine blade, as denoted in Fig. 1b. This enables us to assume a flat unit cell geometry for our FE-mechanical model (Fig. 1d) and CFD-aerothermal model (Fig. 2a1). The effect of inner wall thickness,  $t_c$ , and wall spacing/pedestal height,  $H$ , on the internal aerothermal fields is studied by varying  $H$  for a fixed  $t_c = 1$  mm ( $t_c/D_{imp} = 2.86$  for fixed impingement hole diameter  $D_{imp} = 0.35$  mm), as well as by varying  $t_c$  for  $H = 1.5$  mm ( $H/D_{imp} = 4.29$ ). The remaining geometric ratios are fixed and reported in Table 1. A full thermal solution is obtained by utilising the conjugate method developed by Murray et al [1] and later used by the authors [2,9]. As shown by the schematic in Fig. 2 the method involves the following steps:

**Table 1**

Fixed parameters used in the study.

Unit cell geometry		Aerothermal		Thermal loading		Centrifugal loading	
$D_{film}$	0.2 mm	$T_c$	1000 K	$T_{max}$	1100 °C	$\rho$	8.7e-9 tn/mm <sup>3</sup>
$D_{imp}$	0.35 mm	$m^*$	1, 3, 5	$T_{med}$	1050 °C	$R_{tip}$	400 mm
$D_{ped}$	0.5 mm	$\dot{m}_c/A_{in}$	5.1, 15.2, 25.3 kg/s/m <sup>2</sup>	$T_{min}$	1000 °C	$L$	60 mm
$s$	2.8	$T_\infty$	1870 K				
$w$	1.4	$h$	7500 W/m <sup>2</sup> /K				
$t_h$	1	$P_\infty = P_{s,outlet}$	3.4 MPa				
$\gamma$	60°	$k$	22 W/m/K				
$\rho_{ped}$	30 μm	$c_p$	1006 J/kg/K				
$\rho_{hole}$	10 μm						

1. CFD analysis of internal coolant flow using the unit cell model in Fig. 2a1.

2. Empirical calculation of film effectiveness based on a modified Goldstein-Sellers method (Fig. 2b).

3. FE heat-transfer analysis in an enlarged domain (Fig. 2c), using the results of steps 1 and 2 as input.

Details of the implementation of this scheme are given in Appendix A. Three coolant mass flow rates,  $\dot{m}_c$ , are considered and are expressed by the non-dimensional term,  $m^* = c_p \dot{m}_c / hA$ , where  $c_p$  (J/kg/K) is the specific heat capacity,  $A$  (m<sup>2</sup>) the area subject to external thermal



loading,  $h$  ( $\text{W/m}^2/\text{K}$ ) the external heat transfer coefficient imposed by the external flow. Table 1 gives the prescribed values employed in the CFD model of Fig. 2a1.

## 2.2. Full thermal solution

We first examine the full thermal solution obtained based on the standard unit cell configuration in Fig. 2a1 ( $H/D_{\text{imp}} = 4.29$  and  $t_c/D_{\text{imp}} = 2.86$ ). Fig. 3a shows the contribution of each of the following three regions to internal convective cooling: (a) pedestal and inner wall surfaces, (b) impingement target surface (=inner surface of outer wall) and (c) film hole surfaces. The last of these contributes the most to internal cooling, especially at large coolant flow values,  $m^*$ , given the large heat sink offered by the high outer wall porosity. This suggests that although the impingement jet is important, i.e.  $\sim 20\%$  contribution to internal convective cooling, it can play a secondary role at large  $m^*$ . Nevertheless, for higher external heat fluxes,  $h$ , the impingement jet would act as an important heat sink, limiting elevations in wall temperatures. This is based on the relation of the heat transfer coefficient,  $h = \frac{q}{T_w - T_f}$ , and the impingement jet offers a high heat transfer coefficient, thus any elevations in wall temperature will produce a higher heat flux to counter such increased temperatures.

The cooling performance can be assessed based on the film effectiveness parameter,  $\eta_f = \frac{T_{\infty} - T_{aw}}{T_{\infty} - T_c}$  and/or the cooling effectiveness parameter,  $\epsilon = \frac{T_{\infty} - T_w}{T_{\infty} - T_c}$ , where  $T_{\infty}$  is the external free-stream temperature,  $T_c$  the coolant temperature,  $T_{aw}$  the adiabatic external wall surface temperature and  $T_w$  the temperature at a given wall surface;  $\eta_f$  expresses how well the external surface is cooled by the emerging film jets, whereas  $\epsilon$  signifies the overall cooling performance considering both internal and external flows and is inversely proportional to the temperature at a given wall surface; the minimum value of  $\epsilon$  in the system for each  $m^*$  is given in Table 2a, whereas the temperature profile for the full domain of the transpiration system is shown in Fig. 2c. In principle, transpiration occurs when the solid boundary is in thermal equilibrium with the adjacent fluid, but practically this can be thought to occur when they are within 1 % of the overall driving temperature. In this way we can construct the transpiration factor,  $TF = 1 - \frac{T_w - T_{f, \text{outlet}}}{T_{\infty} - T_c}$ , which is the temperature difference between the wall and fluid divided by the temperature difference between the hot (mainstream) and cold (coolant) flows. Table 2a gives the calculated area-averaged,  $\overline{TF}$ , and maximum transpiration factor,  $\max TF$ , associated with the external hot wall surface, in the investigated  $m^*$  range. It is found that  $\overline{TF} < 0.1$  and that some

**Table 2**

(a) Aerothermal output variables for the unit cell of Fig. 2a1 (geometric ratios of  $t_c/D_{\text{imp}} = 2.86$  and  $H/D_{\text{imp}} = 4.29$ ) for varying non-dimensional mass flow rate,  $m^*$ . (b) Average Nusselt number on the inner surface of the outer wall (impingement target surface) for each geometric combination and mass flow rate  $m^*$ .

$m^*$	1	3	5	6
$\min \epsilon$	0.35	0.51	0.57	0.60
$\Delta T$	191	182	147	130
$\Delta T_{\text{ped}}/\Delta T$	0.59	0.43	0.41	0.4
$\overline{TF}$	0.08	0.10	0.07	0.06
$\max TF$	0.06	0.05	0.02	0.01
$m^*$	1	3	5	
$H/D_{\text{imp}}$	$t_c/D_{\text{imp}}$	$\overline{Nu}$		
0.86	2.86	9.52	24.2	37.6
4.29	2.86	7.93	22.7	36.4
7.14	2.86	7.15	20.4	33.0
4.29	0.57	8.13	23.4	37.8
4.29	1.43	7.99	22.8	36.7
4.29	5.71	7.85	22.6	36.2

locations approach the benchmark  $TF$  of 0.01; the latter depends on  $m^*$  and one may infer that an increase in  $m^*$  may reduce the value further. While transpiration cooling has not been theoretically realised across the majority of the domain and operating conditions, it can be argued that the system of high outer wall porosity studied here acts as a bridge between conventional effusion and transpiration cooling.

## 2.3. Wall spacing and inner wall thickness effects on internal aerothermal field

To explore how the wall spacing/pedestal height influences the above aerothermal results we firstly use the Nusselt number,  $Nu = hD_{\text{imp}}/k$ , defined here as the ratio of convective to conductive heat transfer at the fluid–solid interface of the impingement target surface, where  $h$  ( $\text{W/m}^2/\text{K}$ ) the heat transfer coefficient and  $k$  ( $\text{W/m/K}$ ) the thermal conductivity of the fluid, which is temperature dependent according to kinetic theory. Fig. 4a provides variations of the  $Nu$  contours at the target surface; area-averaged results,  $\overline{Nu}$ , for different geometric combinations and  $m^*$  values are summarised in Table 2b. Wall spacing/pedestal height determines the distance between the impingement jet entry and the target surface, referred to as the target spacing. Reducing this spacing is found to increase the  $Nu$  values in Fig. 4a, resulting in both a higher maximum  $Nu$  at the impingement jet stagnation point and

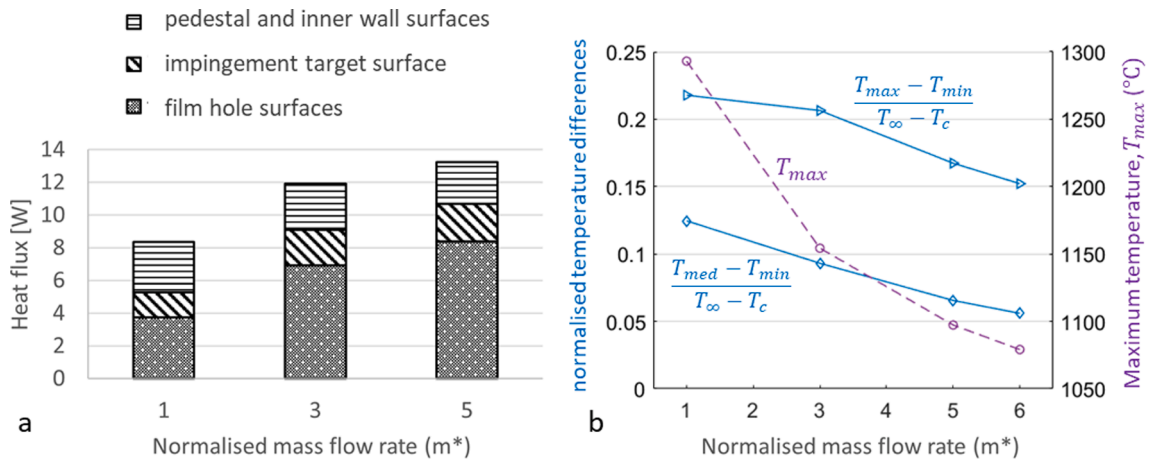


**Fig. 3.** Aerothermal results for the unit cell of Fig. 2a1 (geometric ratios of  $t_c/D_{\text{imp}} = 2.86$  and  $H/D_{\text{imp}} = 4.29$ ). (a) Contribution of the following three regions to internal convective cooling (internal heat flux): film hole surfaces, impingement target surface (=inner surface of outer wall) and pedestal and inner wall surfaces, for varying  $m^*$ . (b) Variation of total normalised thermal difference  $T_{\max} - T_{\min}$  in the system, normalised thermal difference across the pedestal height  $T_{\text{med}} - T_{\min}$  and average maximum temperature  $T_{\max}$  on the external outer wall surface with coolant mass flow rate,  $m^*$ .

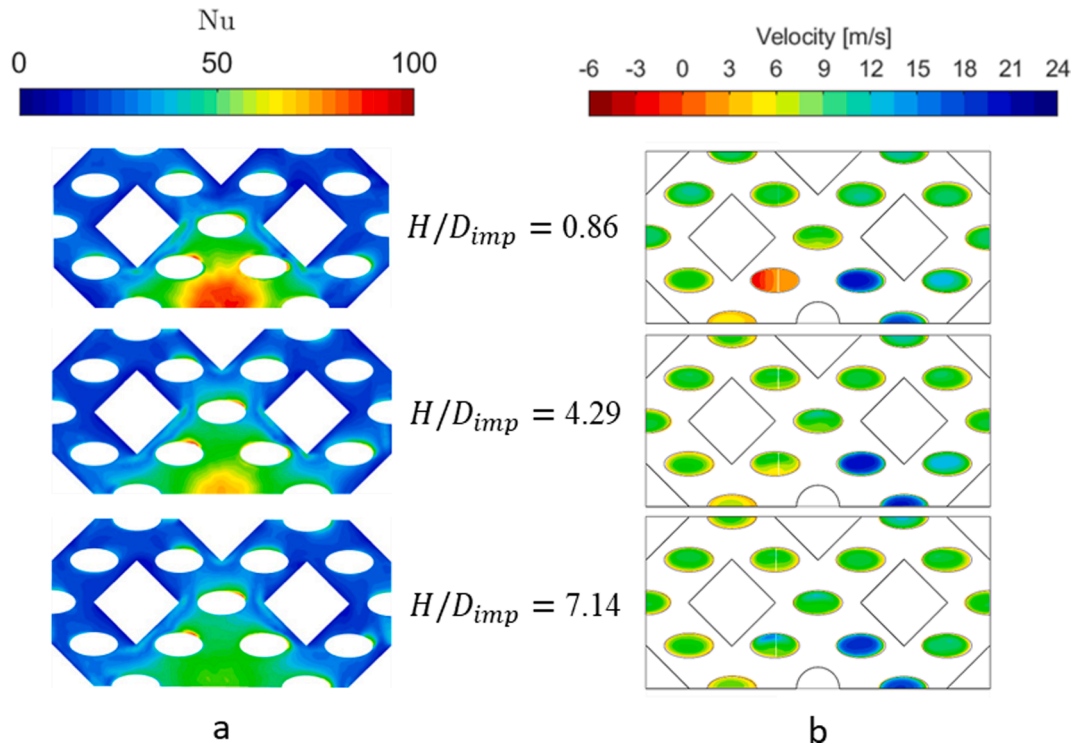


**Fig. 4.** (a) Comparison of Nusselt number contours at the impingement target surface (inner surface of outer wall) for varying pedestal height ratio, (for fixed 2.86 and = 3). b) Velocity contours at film hole exits.

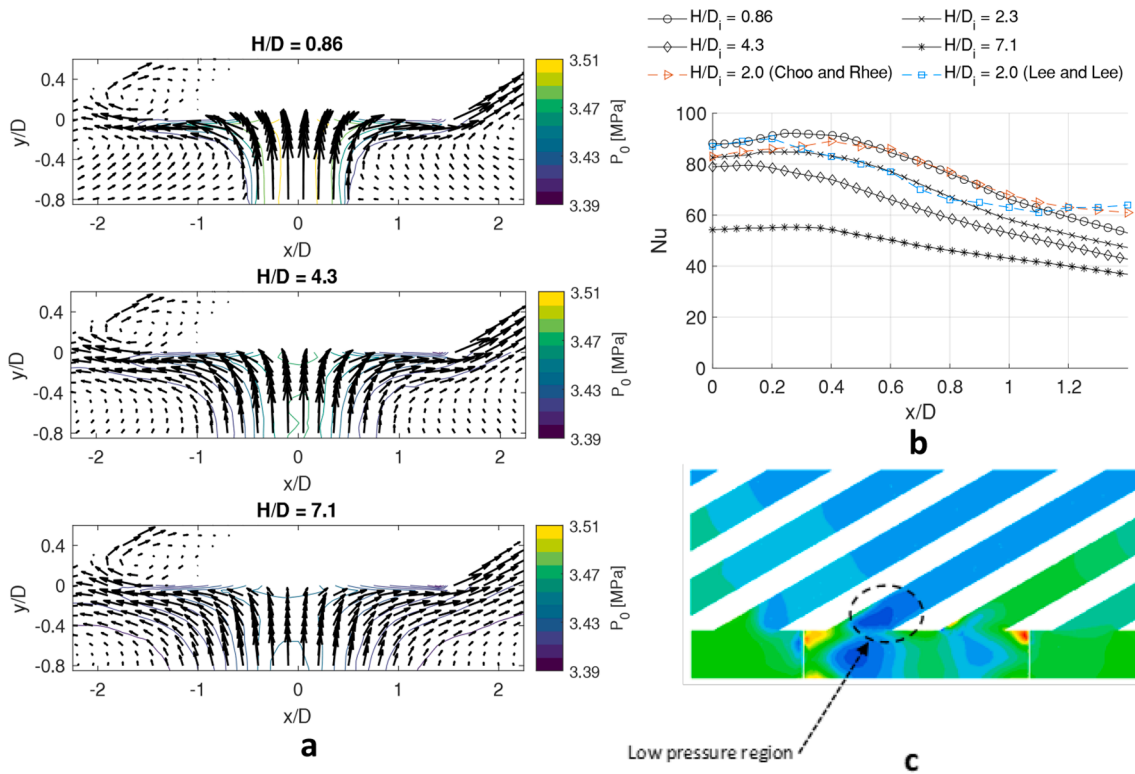


**Fig. 5.** (a) Velocity vectors and total pressure contours for varying pedestal height ratio,  $H/D_{imp}$ , for fixed  $t_c/D_{imp} = 2.86$  and impingement Reynolds number of 10,400 ( $m^* = 3$ ). The influence of impingement target spacing on the impingement jet was observed with a more defined impingement jet and lateral wall for lower  $H/D_{imp}$ . b) Nusselt values on the impingement target surface at  $y/D_{imp} = 0$  plane for varying pedestal height ratio,  $H/D_{imp}$ , for fixed  $t_c/D_{imp} = 2.86$  and impingement Reynolds number of 10,400 ( $m^* = 3$ ). Impingement Nu is plotted for Cho and Rhee (2001) [44] and Lee and Lee (1998) [45] for  $H/D_{imp} = 2.0$  and  $Re_{imp}$  of 10000. c) Pressure within first staggered film holes at  $y/D_{film} = 3.5$  for low pedestal height ( $H/D_{imp} = 0.86$ ). A low-pressure region within the film hole inlet results in an unfavourable pressure gradient, resulting in hot-gas ingestion.

a wider area of elevated heat transfer. As supported by Patil and Vedula [19], the effect is a consequence of: a) the shorter distance travelled by the jet and therefore the fewer opportunities for deterioration of the peak jet velocity, and b) a stronger lateral jet which emerges from the impingement jet stagnation point.

To further understand these assumptions velocity vectors and total pressure contours for three target spacings are displayed in Fig. 5a. The stagnation region of the impingement jet is considered along the symmetry plane ( $y/D_{imp} = 0$ ) and both an upstream and downstream film hole are shown. A deterioration of the peak jet velocity and a widening of the impingement jet was observed for increasing  $H/D_{imp}$ , evidenced by the length of the velocity vectors and the total pressure within the impingement jet region. Given that the film holes are located near the impingement jet stagnation region (less than  $2D_{imp}$ ) it is proposed that this proximity, in conjunction with target spacing, exhibits an influence over the impingement jet shape and intensity. For the case of large  $H/D_{imp}$ , flow can more easily migrate to the film holes, further widening the jet. Conversely, for low  $H/D_{imp}$ , this effect is less pronounced, and the

impingement jet will be more representative of one where the exit flow path is further from the jet core. From a thermal perspective, the effectiveness of the impingement jet is altered and shown in Fig. 5b. We consider the  $Nu$  along a radial line for the impingement target surface for the range of  $H/D_{imp}$ , as well as results from literature (Choo and Rhee [44], Lee and Lee [45]).  $Nu$  in the stagnation region reduced as  $H/D_{imp}$  increased due to the lower impingement and radial wall jet velocity. In agreement with [46] it can be said that the location of effusion holes in relation to impingement jets strongly impacted the heat transfer values. While the results for  $H/D_{imp} \sim 2$  appear representative of measurements in literature, especially in the stagnation region, as radial distance increases the values are lower than those in [44] and [45]. However, a direct comparison poses difficulties as results from the literature rarely consider impingement jets in such proximity to the film holes as well as such a high ratio of film to impingement holes. Given the numerical difficulties with accurate assessment of the impingement jet  $Nu$  as well as geometric differences, the results published here are encouraging, but further study and experimental validation for such geometries should be

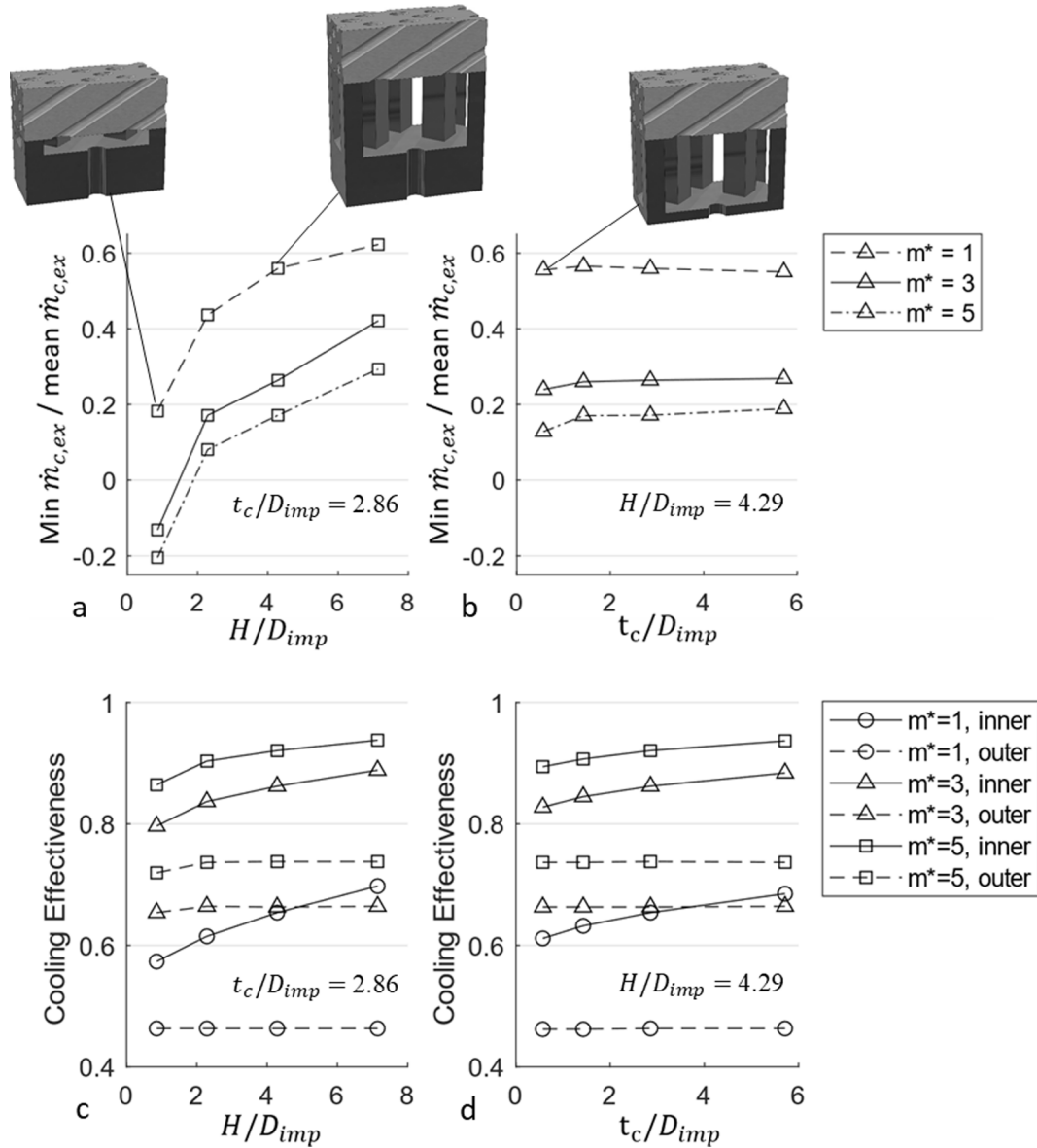


**Fig. 6.** (a) Minimum coolant mass flow at outlets for varying pedestal height  $H/D_{imp}$  ratio and coolant flow  $m^*$ . (b) Minimum coolant mass flow at outlets for varying inner wall thickness  $t_c/D_{imp}$  ratio and coolant flow  $m^*$ . Cooling effectiveness parameter at the outer wall and inner wall external surfaces based on internal convection for: (c) varying pedestal height  $H/D_{imp}$  ratio and coolant flow  $m^*$ , and (d) varying inner wall thickness  $t_c/D_{imp}$  ratio and coolant flow  $m^*$ .

considered in future work.

Despite the benefits of a narrow wall spacing,  $H/D_{imp}$ , on the impingement cooling performance, Fig. 4b shows that the distribution of mass flow to the film holes (velocity contours) is adversely impacted, as it becomes increasingly uneven. This is evidenced by the minimum outlet mass flow results plotted in Fig. 6a. In the worst scenario, hot gas-ingestion is observable for  $H/D_{imp} = 0.86$  and both  $m^* = 3$ ,  $m^* = 5$ , but positive mass flow is shown for the higher  $H/D_{imp}$  cases, with an increase in minimal outlet mass flow. An increase in overall coolant flow reduces the share received by the most deprived film hole, exacerbating the risk of hot-gas ingestion. The discrepancy in coolant flow is explained by the location and orientation of the film hole inlets in relation to the impingement jet stagnation point. For two film holes in close vicinity to this region, there is an inlet with a favourable angle and one with an unfavourable angle compared to the direction of the lateral jet which emerges from the impingement stagnation region, and this can be visualised by the velocity vectors in Fig. 5a. In the former case, the lateral jet needs only turn by the film holes angle of inclination,  $30^\circ$  in this case. However, for the lateral jet moving in the opposite direction to the angle of inclination, a direction change of  $150^\circ$  must be made, and flow separation is more likely. Such a separation on the inner edge of the film holes may result in a low-pressure region within the film hole, and consequently the risk of hot-gas ingestion is increased. At low  $H/D_{imp}$  the impingement jet and, in turn, the lateral jet have increased velocity, hence there is less time and space for these flow corrections to be made. Thus, the flow will favour film holes which impose less of an obstacle. The worst-case scenario is illustrated in Fig. 5c where an unfavourable pressure gradient through the film hole of interest is observed (low pressure region), resulting in hot-gas ingestion.

Importantly, Fig. 6c indicates that the cooling effectiveness parameter at both the external outer wall surface (dashed lines -  $\epsilon = \frac{T_{\infty} - T_{max}}{T_{\infty} - T_c}$ ) and inner wall surface (solid lines -  $\epsilon = \frac{T_{\infty} - T_{min}}{T_{\infty} - T_c}$ ) increases with  $H/D_{imp}$ , particularly at low  $m^*$ ; in the low  $H/D_{imp}$  regime this effect may be partially attributed to the unfavourable effect of poorly fed film holes being stronger than the desirable effect of  $Nu$  increasing at the target surface. Since film holes contribute to most of the convective cooling in the type of systems studied here (Section 2.2), the detriment of hot-gas ingestion can significantly degrade the overall cooling capability and therefore low  $H/D_{imp}$  values should be avoided. This is despite the fact that reducing  $H/D_{imp}$  is shown (Fig. 6c) to alleviate the difference in the cooling effectiveness values at the outer and inner walls (compare solid and dashed lines at each  $m^*$ ), which is proportional to the total temperature difference  $T_{max} - T_{min}$  in the system that drives thermal stresses.

In contrast to the wall spacing/pedestal height, the inner wall thickness is found to have a marginal impact on the flow distribution (see Fig. 6b) and to not cause any hot gas ingestion; a noticeable effect on flow arises only for the aspect ratio below unity, i.e.  $t_c/D_{imp} = 0.57$ . This is consistent with the study by Garimella and Nenaydykh [20] where the impingement hole aspect ratio was observed to have very little influence on  $Nu$  above unity, whereas below unity an increase in both stagnation and average  $Nu$  was observed. It was argued that the separation bubble does not reattach for low aspect ratio holes and reduces the effective hole diameter, leading to an increased jet velocity to maintain continuity and hence higher heat transfer. Despite these benefits, Fig. 6d demonstrates that for the double wall systems considered here the cooling effectiveness in the outer wall (solid lines -  $\epsilon = \frac{T_{\infty} - T_{min}}{T_{\infty} - T_c}$ ) increases with  $t_c/D_{imp}$ , suggesting that the inner wall has a more significant impact on the cooling effectiveness than the  $Nu$  number at the impingement target surface. Similar to the effect of reducing  $H/D_{imp}$  in Fig. 6c, reducing  $t_c/D_{imp}$  in Fig. 6d reduces the difference in cooling effectiveness, and thus the temperature difference between the outer and inner walls.

### 3. Link between aerothermal and mechanical analysis

#### 3.1. Overall strategy

Our next step is to investigate the implications of the above aerothermal results on mechanical performance. The ultimate scope of our study is to identify the full range of possible temperature and stress fields, such that an optimal design can be found that meets both aerothermal and mechanical performance requirements. The aerothermal analysis in Section 2.3 indicates the degree to which the wall spacing/pedestal height,  $H$ , and inner wall thickness,  $t_c$ , influence the cooling effectiveness field and therefore the temperature field. The latter influences the thermal stress field and therefore the mechanical performance. In this context,  $H$  and  $t_c$  have an indirect effect on mechanical performance through their effects on the aerothermal field. A direct effect on mechanical performance is deemed here to occur when thermal stresses vary with geometry without any changes required in the temperature field. This is true here only for  $t_c$ , since the nominal thermal stresses in the walls are effectively invariant with  $H$  for a fixed temperature field; the latter is attributed to the fact that wall rotations are constrained in turbine blade components [15]. This leaves only the geometric parameter  $t_c$  to be varied in the following mechanical analysis in order to characterise its direct effect on the stress field. To highlight the influence of  $t_c$ , in this analysis the temperature field is kept fixed.

The indirect effects of  $H$  and  $t_c$  on the stress field will not be studied explicitly here; this would require a different temperature field to be prescribed in the FE model of Fig. 1d for each  $H - t_c$  combination. A more efficient strategy is to idealise the temperature field such that it can be described by three parameters: the peak temperature in the system  $T_{max}$ , the total temperature difference  $\Delta T = T_{max} - T_{min}$  across the double walls and the difference  $\Delta T_{ped} = T_{med} - T_{min}$  across the pedestal height (see Fig. 1d). The relationship between  $\Delta T$  and the values of  $H$ ,  $t_c$  can be evaluated from the cooling effectiveness results in Fig. 6c-d; the effect of  $H$  and  $t_c$  on  $\Delta T_{ped}$  and its importance on thermal stresses is not significant and can be reasonably ignored. A single mechanical FE simulation for a typical temperature field can then determine how stresses scale with  $\Delta T$ . With this information, any modifications of the temperature field, i.e. of the parameter  $\Delta T$ , induced by changes of  $H$  and/or  $t_c$  can be readily translated into changes in stresses. The idealisation of the temperature field has an additional merit. It allows for analytical stress solutions to be generated, which will be used here to understand the role of key parameters in the problem (e.g. wall thickness ratio, crystal orientation, thermoelastic material properties) as well as to interpret the FE results. The validity of idealising the temperature field for the purposes described above was demonstrated in [2,21], on the basis that high order temperature perturbations play a minor role in determining the thermal stresses. This observation was made for systems of modest outer wall porosity (Fig. 2a2) and it is reasonably assumed to also hold for the high porosity systems considered here (Fig. 2a1).

#### 3.2. Using the aerothermal output

We now interpret the temperature field results in the context of mechanical performance and choose a typical fixed temperature field for use in the mechanical analysis. The three temperature field parameters,  $T_{max}$ ,  $\Delta T$  and  $\Delta T_{ped}$  are given as a function of  $m^*$  in Fig. 3b (note:  $\Delta T$  and  $\Delta T_{ped}$  are normalised by  $T_{\infty} - T_c$ ) and Table 2a.  $\Delta T$  is known to be the main thermal quantity that determines the magnitude of the thermal stresses, whereas  $\Delta T_{ped} = T_{med} - T_{min}$  has been found to have a second order effect [2,22]; that is, the membrane stresses dominate over bending stresses in the hot wall as  $\Delta T_{ped}/\Delta T$  increases. Although this implies a small increase in tensile stresses in the cool wall, a more significant reduction in compressive stresses in the outer hot wall surface occurs, such that high  $\Delta T_{ped}/\Delta T$  can be deemed beneficial to mechanical performance in most cases [2]. In this regard, Table 2a implies that a



lower  $m^*$  is beneficial. However, the variation of  $\Delta T_{ped}/\Delta T$  in the  $m^*$  range is found to be relatively small and its effect on stresses is generally far less important than the effect of  $\Delta T$ . In fact, a large  $m^*$  is favourable, not only because it reduces  $\Delta T$  (Table 2a) but also because it reduces the peak metal temperature,  $T_{max}$ ; the latter is important because the elastoplastic properties of Ni-alloys degrade sharply at temperatures  $T > 700$  °C.

Based on the above, a representative temperature field for use in the mechanical analysis could correspond to  $m^* = 5$ , with parameters  $T_{max} = 1100$  °C,  $\Delta T = 147$  °C and  $\Delta T_{ped}/\Delta T = 0.41$ . However, engine efficiency requirements may pose a limit to the maximum value of  $m^*$  that can be used in practice, and it is generally difficult to know a priori the exact value of  $m^*$  and corresponding temperature field. Furthermore, our primary aim here is to determine how stresses scale with  $\Delta T$  in the elastic range, and because of the linear nature of the problem an arbitrary value of  $\Delta T$  can be used in the mechanical analysis. In this regard, we use a standard set of parameters  $T_{max} = 1100$  °C,  $\Delta T = 100$  °C and  $\Delta T_{ped}/\Delta T = 0.5$  (i.e.  $T_{med} = 1050$  °C,  $T_{min} = 1000$  °C). When evaluating the results of the analysis, the scaling factor  $\Delta T$  is replaced by the reference thermal stress,  $\sigma_T = \kappa \bar{E} \alpha \Delta T / (1 - \bar{\nu}) = 318$  MPa, where  $\bar{E} = 150$  GPa,  $\bar{\nu} = 0.34$  and  $\alpha = 2 \times 10^{-5}$  are isotropic CMSX-4 properties for 1050 °C,  $\Delta T = 100$  °C,  $\bar{\nu} = 0.5$  is the ratio of an individual wall thickness over the sum of wall thicknesses and  $\kappa = 1.4$  is a scaling factor associated with the temperature dependence of thermoelastic properties,  $\alpha$ ,  $\bar{E}$ ,  $\bar{\nu}$  [22]. The derivation of  $\sigma_T$  above is based on an analytical thermal stress field solution for isotropic elastic double plates and is detailed by the authors in [23].

## 4. Mechanical analysis

### 4.1. Material model for CMSX-4 alloy

We consider the thermoelastic properties of the CMSX-4 alloy shown in Fig. 7. These include an isotropic thermal expansion coefficient,  $\alpha$ , which increases with temperature,  $T$ , and three independent stiffness constants,  $C_{11}$ ,  $C_{12}$ ,  $C_{44}$  which decrease with  $T$ ; each constant decreases in a different manner such that the degree of elastic anisotropy represented by the Zener factor,  $A = 2C_{44}/(C_{11} - C_{12})$ , increases with  $T$ ;  $A$  is the ratio of shear moduli corresponding to the  $\langle 100 \rangle$  and  $\langle 110 \rangle$  crystallographic directions [24]. The Young's modulus,  $\hat{C}_{11}$ , and compliance,  $\hat{S}_{11}$ , along a direction with cosines,  $l_1$ ,  $l_2$ ,  $l_3$  relative to the principal crystal axes [001], [010], [100] (shown in Fig. 7b) obey the relation  $1/$

$\hat{C}_{11} = \hat{S}_{11} = S_{11} + \ell S_{44}(1 - A)$ , where  $S_{11}$ ,  $S_{44}$  are compliance constants defined in Appendix B and  $\ell = l_1^2 l_2^2 + l_2^2 l_3^2 + l_3^2 l_1^2$ ;  $\ell = 0$  along the three cube normal directions  $\langle 100 \rangle$ ,  $\ell = 1/4$  along the six cube face diagonals  $\langle 110 \rangle$  and  $\ell = 1/3$  along the four cube diagonals  $\langle 111 \rangle$ . For Fig. 6a this implies that at a typical temperature of interest,  $T \approx 1000$  °C, the  $\langle 110 \rangle$  and  $\langle 111 \rangle$  directions are 1.95 and 2.85 times stiffer than  $\langle 100 \rangle$ , whereas the volume averaged Young's modulus,  $\bar{E}$ , is 1.9 times higher than that along  $\langle 100 \rangle$ . The volume averaged modulus  $\bar{E}$  and Poisson's ratio  $\bar{\nu}$  are computed in Appendix C and will be used here to represent the case of a polycrystalline CMSX-4 where a large number of grains with different orientations statistically gives an isotropic macroscopic response.

### 4.2. Thermal stresses in a double wall turbine blade

Prior to analysing the detailed stress field in the repeating unit of Fig. 1d, it is essential to firstly determine stresses in the double wall turbine blade model of Fig. 1a-b. This allows us to capture anisotropic effects associated with single crystal blades that cannot be captured by a unit cell model with constant curvature, as well as to identify the overall nature of the nominal thermal stresses in the real component and justify the kinematic boundary conditions to be used in a subsequent unit cell analysis. component of interest justify the in repeating A blade length of 60 mm and 1 mm uniform wall thicknesses and wall spacing are used; the blade is supported at the fir-tree region in which zero y-displacements and z-displacements are applied on its lateral surfaces (denoted in blue in Fig. 1a) and zero x-displacement on its front surface (denoted in red in Fig. 1a). Pedestals are not modelled discretely but instead their presence is mimicked through enforcing zero relative  $x$ ,  $y$ ,  $z$  displacements between each node at the inner hot wall surface and its adjacent node at the inner cool wall surface. We prescribe the temperatures  $T_{max} = 1100$  °C and  $T_{med} = 1050$  °C at the outer and inner surface of the hot wall and  $T_{min} = 1000$  °C at the entire cool wall (temperature field justified in Section 3.2), in a uniform manner along the streamwise,  $\xi$ , and spanwise,  $z$ , directions of the blade (see Fig. 1b). A detailed description of the blade model in Fig. 1a-b is given in a previous report [2] where thermal, centrifugal (CF) and aerodynamic bending (P) stresses were studied for an isotropic material. Here we explore how thermal stresses occur when the elastic anisotropy of the CMSX-4 alloy comes into play.

The orientation of the principal crystal axes (Fig. 1c) with respect to the global blade system XYZ (Fig. 1a-b) is defined by a sequence of three intrinsic rotations of type ZXZ' [25] by the Euler angles,  $\varphi$ ,  $\theta$ ,  $\psi$ ; the

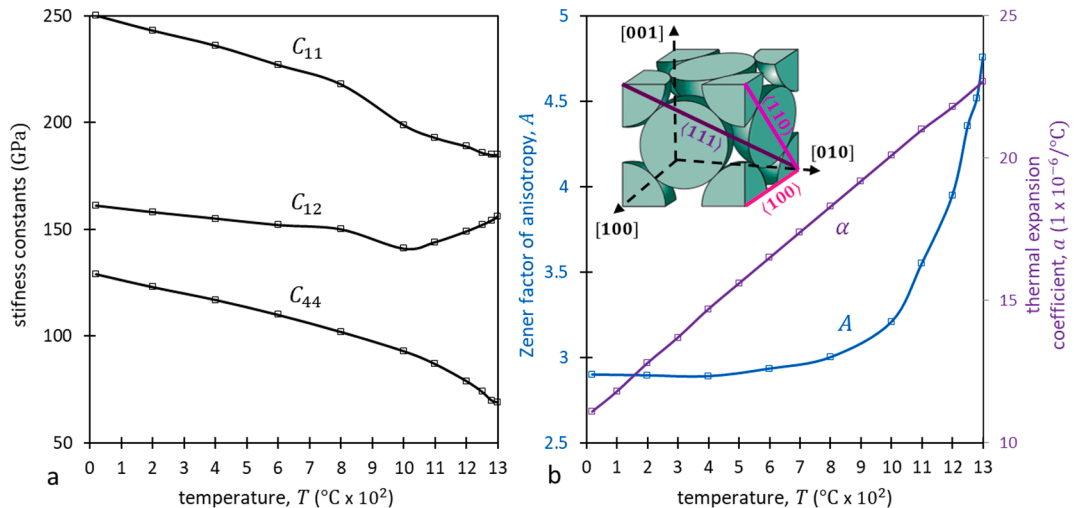


Fig. 7. Thermoelastic properties of the CMSX-4 alloy. (a) Stiffness constants versus temperature (taken from [3]). (b) Zener factor of anisotropy and coefficient of thermal expansion (taken from [4]).

angle  $\theta$  defines the cone illustrated in Fig. 3b; the transformation matrix between the crystal and blade systems is given in Appendix B. In current manufacturing procedures only  $\theta$  is controlled, with the target value being  $\theta = 0^\circ$  such that  $\langle 100 \rangle$  aligns with the blade axis Z; blades that do not satisfy  $\theta \leq 15^\circ$  are rejected. The randomness of  $\varphi$  and  $\psi$  angles implies that different blades exhibit different mechanical behaviour. This is evident here by comparing the thermal stress field at a representative blade cross-section (15 mm away from the blade root) between the cases of no crystal rotation (Fig. 8a-b) and a crystal rotation of  $\varphi = 45^\circ$  (Fig. 8c-d); in Fig. 8e-f we also plot results for polycrystalline CMSX-4 where the stresses are higher since the volume averaged  $\bar{E}$  and  $\bar{\nu}$  properties are used.

Before explaining the orientation effect, it is important to recognize that for the thin wall structures considered here stresses effectively arise only in the wall planes. The cool wall is in pure tension and therefore experiences positive maximum and intermediate principal stress, i.e.  $\sigma_1 > 0$  and  $\sigma_2 > 0$ , ( $\sigma_3 \approx 0$ ), whereas the hot wall is subjected to membrane compression combined with bending such that the in-plane principal stresses are compressive,  $\sigma_2 < 0$  and  $\sigma_3 < 0$  in its outer fibres and the out of plane principal stress,  $\sigma_1 \approx 0$ . To best illustrate these characteristics we plot the maximum absolute principal stresses,  $\sigma = \max(\sigma_1, |\sigma_3|)$ , in Fig. 8a,c,e and intermediate principal stresses,  $\sigma = \sigma_2$ , in Fig. 8b,d,f, and normalise them with respect to the reference thermal stress,  $\sigma_T$  defined in Section 3. The  $\sigma_2$  stresses are approximately equal to the stresses along the global blade axis, Z, i.e.  $\sigma = \sigma_2 \approx \sigma_z$  in Fig. 8b,d,f, whereas the maximum absolute principal stresses are approximately equal to the stresses along the blade chord/streamwise,  $\xi$ , blade direction, i.e.  $\sigma = \max(|\sigma_1|, |\sigma_3|) \approx \sigma_\xi$  in Fig. 8a,c,e. These features apply along almost the entire blade length because a uniform temperature field is prescribed and therefore any variation in the stress field effectively occurs only near the blade root and the blade tip regions.

An effect that occurs regardless of anisotropy is that at the highly curved regions of the blade the  $\sigma_\xi$  stresses are higher than  $\sigma_z$  stresses (see Fig. 8e-f); such effects have been explained in [22]. The major effect induced by anisotropy (Fig. 8a-d) is that the  $\sigma_z$  stresses lie along the  $[001]$  direction (due to  $\theta = 0^\circ$ ) and therefore are much lower than the  $\sigma_\xi$  stresses which are highest in regions where the direction of  $\sigma_\xi$  aligns

with the  $[110]$  direction (as denoted in Fig. 8a). This alignment generally occurs at different blade regions for different rotations,  $\varphi$  (note that  $\varphi \equiv \psi$  when  $\theta = 0^\circ$ ), which in combination with the aforementioned curvature effect leads here to a better overall mechanical response in Fig. 8c-d for  $\varphi = 45^\circ$  compared to Fig. 8a-b for  $\varphi = 0^\circ$ . In this regard, various authors have looked at optimising the crystal orientation for specific blade geometries based on parametric FE analysis [26–28]; however, theoretical solution are not available that provide physical insight into the orientation effect for thin wall systems and none of these studies have considered the effect of stress raising features, i.e. holes and pedestals, which are important stress raising features of the double wall transpiration cooling systems considered here. These aspects will be addressed in Sections 4.3 and 4.4.

#### 4.3. Thermal stresses in flat double plates

To aid the development of theoretical solutions for nominal stresses (in the absence of holes and pedestals) we ignore wall curvature effects and utilise the idealised flat unit cell in Fig. 1d for a variable crystal orientation. Consider the system  $xyz$  which is local to the turbine blade (Fig. 1a-b) and global to the unit cell (Fig. 1d). The kinematic requirement of equal total strains between the walls in  $x$  the direction gives:

$$\frac{s_h^M x}{t_h} \int_{-\frac{t_h}{2}}^{\frac{t_h}{2}} \hat{S}_{11}(T(y)) dy + \frac{s_h^M z}{t_h} \int_{-\frac{t_h}{2}}^{\frac{t_h}{2}} \hat{S}_{13}(T(y)) dy + \frac{1}{t_h} \int_{-\frac{t_h}{2}}^{\frac{t_h}{2}} \alpha(T(y)) T(y) dy = s_{cx} \hat{S}_{11}(T_{min}) + s_{cz} \hat{S}_{13}(T_{min}) + a T_{min}(a)$$

The same requirement for the  $z$  direction gives:

$$\frac{s_h^M x}{t_h} \int_{-\frac{t_h}{2}}^{\frac{t_h}{2}} \hat{S}_{31}(T(y)) dy + \frac{s_h^M z}{t_h} \int_{-\frac{t_h}{2}}^{\frac{t_h}{2}} \hat{S}_{33}(T(y)) dy + \frac{1}{t_h} \int_{-\frac{t_h}{2}}^{\frac{t_h}{2}} \alpha(T(y)) T(y) dy = s_{cx} \hat{S}_{31}(T_{min}) + s_{cz} \hat{S}_{33}(T_{min}) + a T_{min}(b)$$

Equilibrium along  $x$  and  $z$  respectively gives: (1)

$$s_h^M x t_h + s_{cx} t_c = 0(c)$$

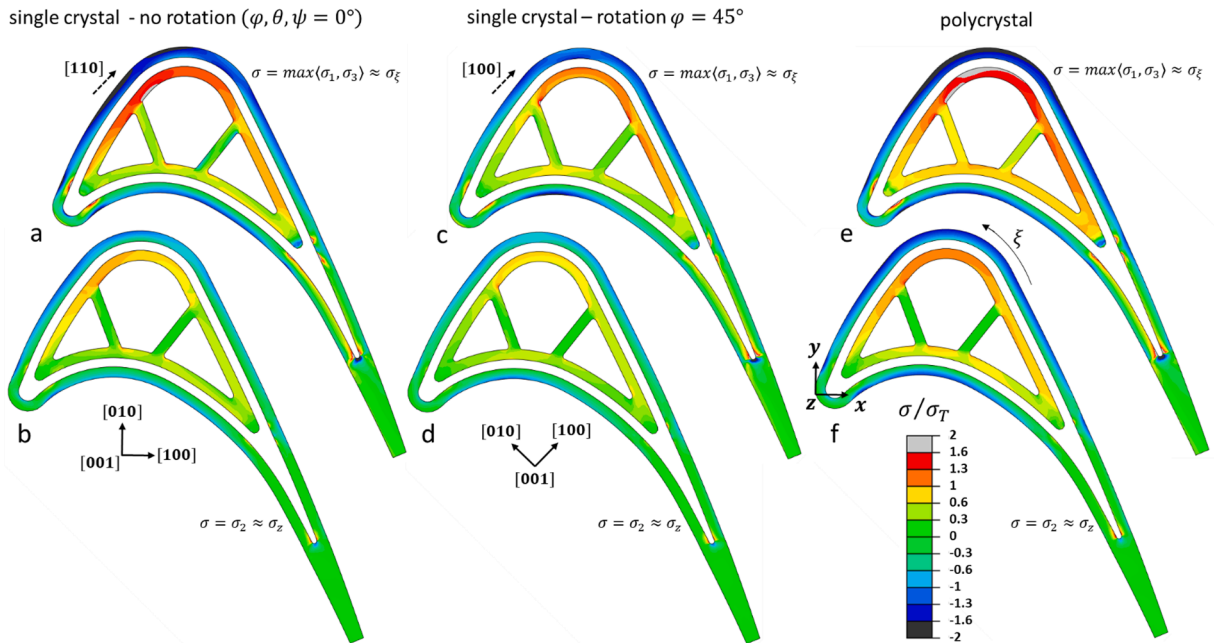


**Fig. 8.** Thermal stress fields at the cross-section of the turbine blade model of Fig. 1b, 15 away from the blade root. (a-b) A single crystal CMSX-4 blade with no crystal rotation with respect to the blade system. (c-d) A crystal rotation of  $\varphi = 45^\circ$ . (e-f) A polycrystalline (isotropic) blade where volume averaged properties of CMSX4 are used. Fig. 7a,c,e show maximum absolute principal stresses; Fig. 7b,d,f show intermediate principal stresses; all stresses are normalised by the reference stress,  $\sigma_T = 318$  MPa.

$$s_h^M z t_h + s_c z t_c = 0(d)$$

where  $s_h^M x$ ,  $s_h^M z$  are the nominal membrane thermal stresses in the hot wall along  $x$  and  $z$ ,  $s_{cx}$ ,  $s_{cz}$  are the corresponding cool wall stresses,  $t_h$ ,  $t_c$  are the hot and cool wall thicknesses and the terms  $\hat{S}_{ij}$  are components of

the compliance matrix  $\hat{S}$  in the  $xyz$  system, which is related to the material compliance,  $S$ , according to  $\hat{S} = \bar{T}^T S \bar{T}$ , where the transformation matrix,  $\bar{T}$ , is constructed based on the Euler angles,  $\varphi$ ,  $\theta$ ,  $\psi$  in Appendix B. Since the temperature,  $T$ , varies with position,  $y$ , through the thickness

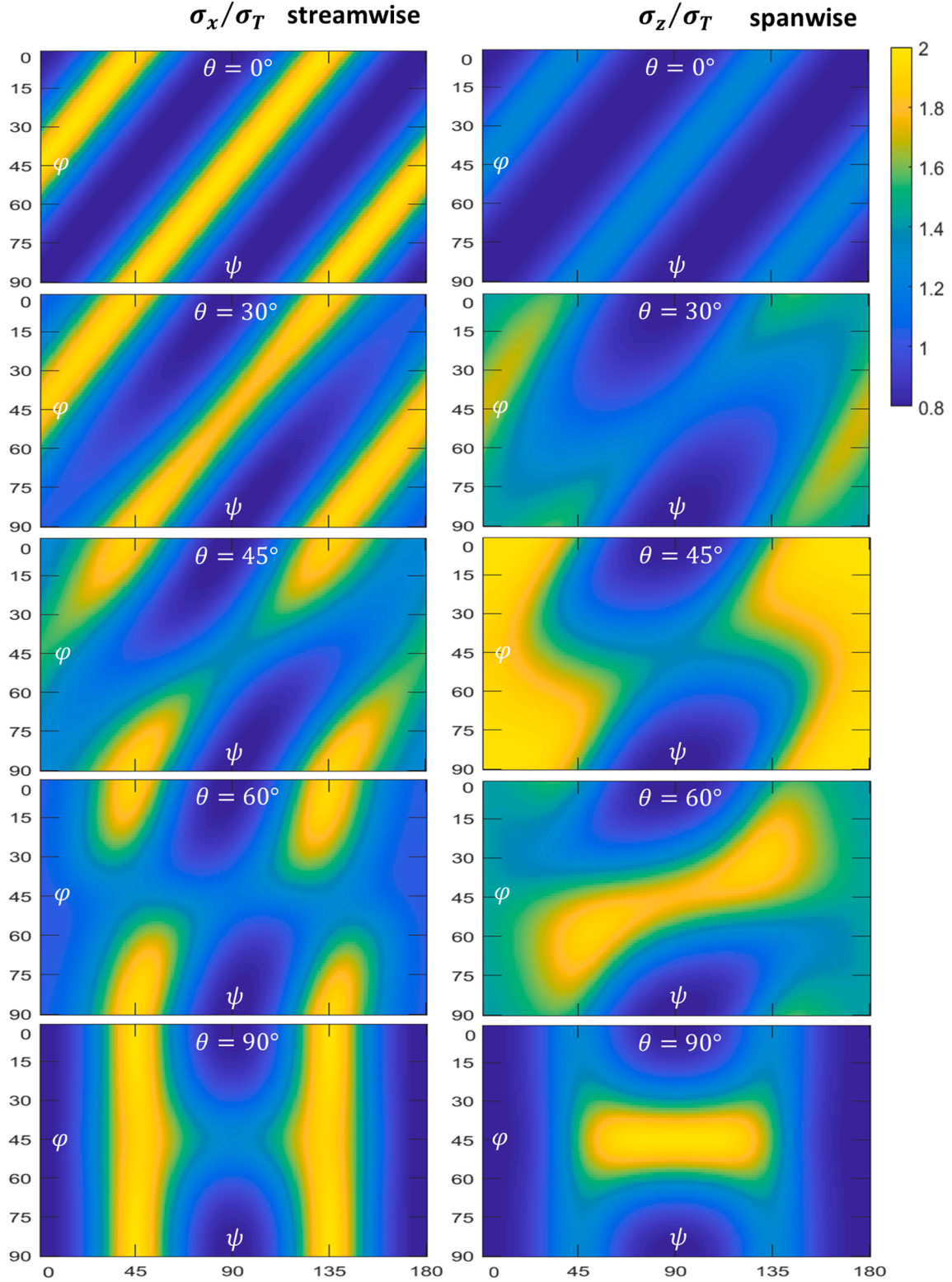


**Fig. 9.** Variation of the magnitude of the nominal compressive thermal stress at the outer fibre of the hot wall along the  $x$  and  $z$  directions in the system of Fig. 1d, with respect to the crystal rotation (Euler) angles,  $\varphi$ ,  $\theta$ ,  $\psi$ . Stresses are computed theoretically through Eqs 1–3 ( $p_{CF} = 0$ ) and are normalised over the reference thermal stress,  $\sigma_T = 318$  MPa;  $x$  and  $z$  correspond to the streamwise and spanwise directions of the blade in Fig. 1b.



of the hot wall,  $\hat{S}_{ij}$  and  $a$  are both functions of  $T(y)$  on the LHS of Eqs 1a-b, whereas on the RHS of Eqs 1a-b they have constant values since the cool wall is at uniform temperature,  $T_{min}$ . Bending stresses,  $s_h^B(x(y), s_h^B(z(y))$ , in the hot wall due to the temperature variation  $T(y)$  are determined by postulating zero total bending curvatures about  $z$  and  $x$  axes, which respectively gives:

$$\frac{M_{hx}}{I} \int_{-\frac{t_h}{2}}^{\frac{t_h}{2}} \hat{S}_{11}(T(y))y^2 dy + \frac{M_{hz}}{I} \int_{-\frac{t_h}{2}}^{\frac{t_h}{2}} \hat{S}_{13}(T(y))y^2 dy + \int_{-\frac{t_h}{2}}^{\frac{t_h}{2}} \alpha(T(y))T(y)y dy = 0(a)$$

(2)

$$\frac{M_{hx}}{I} \int_{-\frac{t_h}{2}}^{\frac{t_h}{2}} \hat{S}_{31}(T(y))y^2 dy + \frac{M_{hz}}{I} \int_{-\frac{t_h}{2}}^{\frac{t_h}{2}} \hat{S}_{33}(T(y))y^2 dy + \int_{-\frac{t_h}{2}}^{\frac{t_h}{2}} \alpha(T(y))T(y)y dy = 0(b)$$

where  $I = t_h^3/12$  is the second moment of area per unit length and  $M_{hx}$ ,  $M_{hz}$  are the bending moments about  $x$  and  $z$ , such that  $s_h^B(x(y) = M_{hx}y/I$  and  $s_h^B(z(y) = M_{hz}y/I$ . By superimposing a uniform centrifugal  $z$ -stress,  $p_{CF}$ , the resulting nominal stresses are:

$$\sigma_{hx}(y) = s_h^M x + s_h^B x(y) \text{ and } \sigma_{hz}(y) = s_h^M z + s_h^B z(y) + p_{CF}(a)$$

(3)

$$\sigma_{cx} = s_{cx} \text{ and } \sigma_{cz} = s_{cz} + p_{CF}(b)$$

We now utilise Eqs 1–3 to reveal the effect of crystal orientation on the compressive nominal stress magnitude at the external surface of the hot wall,  $\sigma_{hx}(y = -t_h/2)$  and  $\sigma_{hz}(y = -t_h/2)$ , for the full range of Euler angles  $\varphi$ ,  $\theta$ ,  $\psi$ . We consider the same temperature field used in Section 4.2 with  $T_{max} = 1100^\circ\text{C}$ ,  $T_{med} = 1050^\circ\text{C}$  and  $T_{min} = 1000^\circ\text{C}$ . The results are illustrated in Fig. 8 in terms of absolute values normalised by the reference thermal stress,  $\sigma_T = 318$  MPa. First, we recognise that for  $\theta = 0^\circ$  the  $\varphi$  rotation is equivalent to the  $\psi$  rotation; in this case, the entire range of behaviour can be studied by varying  $\varphi$  or  $\psi$  between  $0^\circ$  and  $45^\circ$  and the  $x$  – stresses and  $z$  – stresses can only align with the  $\langle 100 \rangle$  or  $\langle 110 \rangle$  crystal axes. For  $\theta > 0^\circ$  the effect of orientation becomes more complex. The  $z$  – stresses (aligned with  $Z$  blade axis in Fig. 1b), generally take small values for low  $\theta$  (see Fig. 9), since in this range the stresses act approximately along the compliant  $\langle 001 \rangle$  crystal axis; note however that even for  $\theta = 0^\circ$  the  $z$  – stresses slightly increase when  $x$  – stresses increase, as the two components are coupled by Hooke's law (Eqs 1a-b). It appears that the worst scenario in terms of  $z$  – stresses in the turbine blade is when  $\theta = 45^\circ$  (see Fig. 9) because these are a maximum for many combinations of  $\varphi$  and  $\psi$  due to alignment of the stiff  $\langle 111 \rangle$  crystal direction with the  $z$  direction.

These results justify the use of a maximum permissible value of  $\theta = 15^\circ$  by the current manufacturing practise. Additional FE simulations for this extreme ( $\theta = 15^\circ$ ) using the blade model in Fig. 1b show that the results in Fig. 8a-b are not significantly modified. Conclusively, our design problem here is mainly concerned with orientation effects associated with the variation of  $\varphi$  between  $0^\circ$  and  $45^\circ$  and this variation will be our main consideration in the following FE analysis of stresses at features.

#### 4.4. Thermal and centrifugal stresses in a DWTC system

We now study local stresses at holes and pedestals in Fig. 1d for a wide range of practical thermal-centrifugal load combinations. We firstly need to acknowledge that centrifugal (CF) stresses,  $p_{CF}$ , generally vary along the spanwise  $Z$  blade axis between zero at the tip of a blade to a maximum value at the root. As a result, for the purposes of this study we will use a fixed temperature field and vary  $p_{CF}$ . In particular, we apply the same temperatures uniformly along the walls used in Section 4.2 ( $T_{max} = 1100^\circ\text{C}$ ,  $T_{med} = 1050^\circ\text{C}$ ,  $T_{min} = 1000^\circ\text{C}$  - see Fig. 1d) and vary  $p_{CF}$  in the range 0 – 300 MPa, such that  $p_{CF}/\sigma_T$  ranges from 0 to  $\sim 1$

( $\sigma_T = 318$  MPa); the validity of using the idealised temperature field of Fig. 1d in which temperatures do not vary along the wall planes has been demonstrated in [2]. Here  $p_{CF}$  is the nominal CF stress carried by the gross wall sections and is introduced in Fig. 1d in the form of an equivalent uniform traction  $p_{CFnet}$  ( $< p_{CF}$ ) at the  $\bar{z} = 1$  plane, throughout the reduced/net sections of the walls. The calculation of  $p_{CFnet}$  based on turbine rotational speed (rpm), material density and transpiration cooling geometry is provided in Appendix D. In terms of displacement boundary conditions, we apply zero  $z$  – displacements at the  $\bar{z} = 0$  plane, common  $z$  – displacement for all nodes at  $\bar{z} = 1$  and periodic conditions at the pair of  $\bar{x} = 0$ ,  $\bar{x} = 1$  planes; note that here  $\bar{z} = 0$  and  $\bar{z} = 1$  are symmetry planes because the crystal is rotated only about the  $\varphi$  axis (see Fig. 1d).

Our results are summarised in Figs. 10–11. Firstly, for a typical combination of  $\varphi = 45^\circ$  and  $p_{CF} = 225$  MPa in Fig. 10a-c we indicate that the resulting  $\max(|\sigma_1|, |\sigma_3|)$  stress field (Fig. 10c) is given by superposition of the thermal (Fig. 10a) and CF (Fig. 10b) stress fields. The detailed distribution of stress at features for the same thermal-CF loading combination is illustrated in Fig. 10a-f in terms of maximum absolute resolved shear stress,  $\max(|\tau_{rss}|)$ , amongst the 12 octahedral slip systems  $\{111\}\langle 110 \rangle$  of the FCC lattice, with the  $\tau_{rss}$  vector (12x1) given by Schmid's law as  $\tau_{rss} = \sigma : (s \otimes n)$ , where  $\sigma$  is the stress tensor (3x3) in the crystal system and  $s$ ,  $n$  are the matrices (12x3) containing unit vectors normal to the slip planes and unit vectors in the direction of slip, respectively. By taking the peak value  $\max(|\tau_{rss}|)$  at each feature and normalising it by the range of the critically resolved shear stress during cycling between the hot and cold temperatures,  $\Delta\tau_{crss} = \tau_{crssT} + \tau_{crss0}$ , we construct the plots in Fig. 11a1-c1, where the ratio  $\frac{\max(|\tau_{rss}|)}{\Delta\tau_{crss}}$  indicates the degree by which local reversed plastic straining would occur in practice, which provides a measure of the likelihood of the development of fatigue damage; the calculation of  $\Delta\tau_{crss}$  based on the critical resolved shear stress at high temperature,  $\tau_{crssT}$  (full thermal loading) and at room temperature,  $\tau_{crss0}$  (zero loading) is provided in Appendix E.

From a practical perspective, conclusions about fatigue performance may be drawn based on Fig. 11a1-c1 alone. The following effects are observed:

A. A thinner cool wall ( $t_c/t_h = 0.5$ ) reduces film hole stresses at the cost of increasing stresses at internal features, i.e. impingement hole and pedestal.

B. Hole stresses are higher for  $\varphi = 45^\circ$  compared to  $\varphi = 0^\circ$  (Fig. 11a1-b1) whereas slightly the opposite is shown for the pedestal stresses (Fig. 11c1).

C. CF loading generally increases stresses at internal features (Fig. 11b1-c1) whereas film hole stresses (Fig. 11a1) initially reduce in the low  $p_{CF}$  regime and then increase in the high  $p_{CF}$  regime.

In order to interpret these effects we can consider that  $\max(|\tau_{rss}|)$  scales with the peak compressive stress magnitude,  $|\sigma_3|$ , at the film hole and the peak tensile stress,  $\sigma_1$ , at the impingement hole and the pedestal. Both  $|\sigma_3|$  and  $\sigma_1$  are found to: a) occur at approximately the same location at each feature as the peak value of  $\max(|\tau_{rss}|)$  (not shown), and b) to vary in a similar manner with respect to the  $p_{CF}/\sigma_T$  and  $t_c/t_h$  ratios as well as the rotation,  $\varphi$ . We also note that the elastic stress state at the locations of the peak stress at the holes is effectively uniaxial and involves a principal stress in the  $x$ – $z$  plane which is tangent to the circumference of the rim of each hole, i.e.  $\sigma_1, \sigma_2 \approx 0$  at the film hole (compression) and  $\sigma_2, \sigma_3 \approx 0$  at the impingement hole (tension). In contrast, the pedestal fillet experiences a biaxial state as the  $\sigma_1$  component (which is transversely tangent to the fillet in Fig. 10f) is accompanied by a  $\sigma_2$  component which is circumferentially tangent to the filleted corner. All the above suggest that the  $\max(|\tau_{rss}|)$  results can be interpreted based on the  $|\sigma_3|$  behaviour at the film hole and the  $\sigma_1$  behaviour at the impingement hole and pedestal.

In order to fully explain the effects described in A, B and C, we note that  $|\sigma_3|$  and  $\sigma_1$  can be expressed as:

$$\text{film hole: } |\sigma_3| = |\sigma_{hx}(y = -t_h/2)| \bullet SCF_{film}(4a)$$



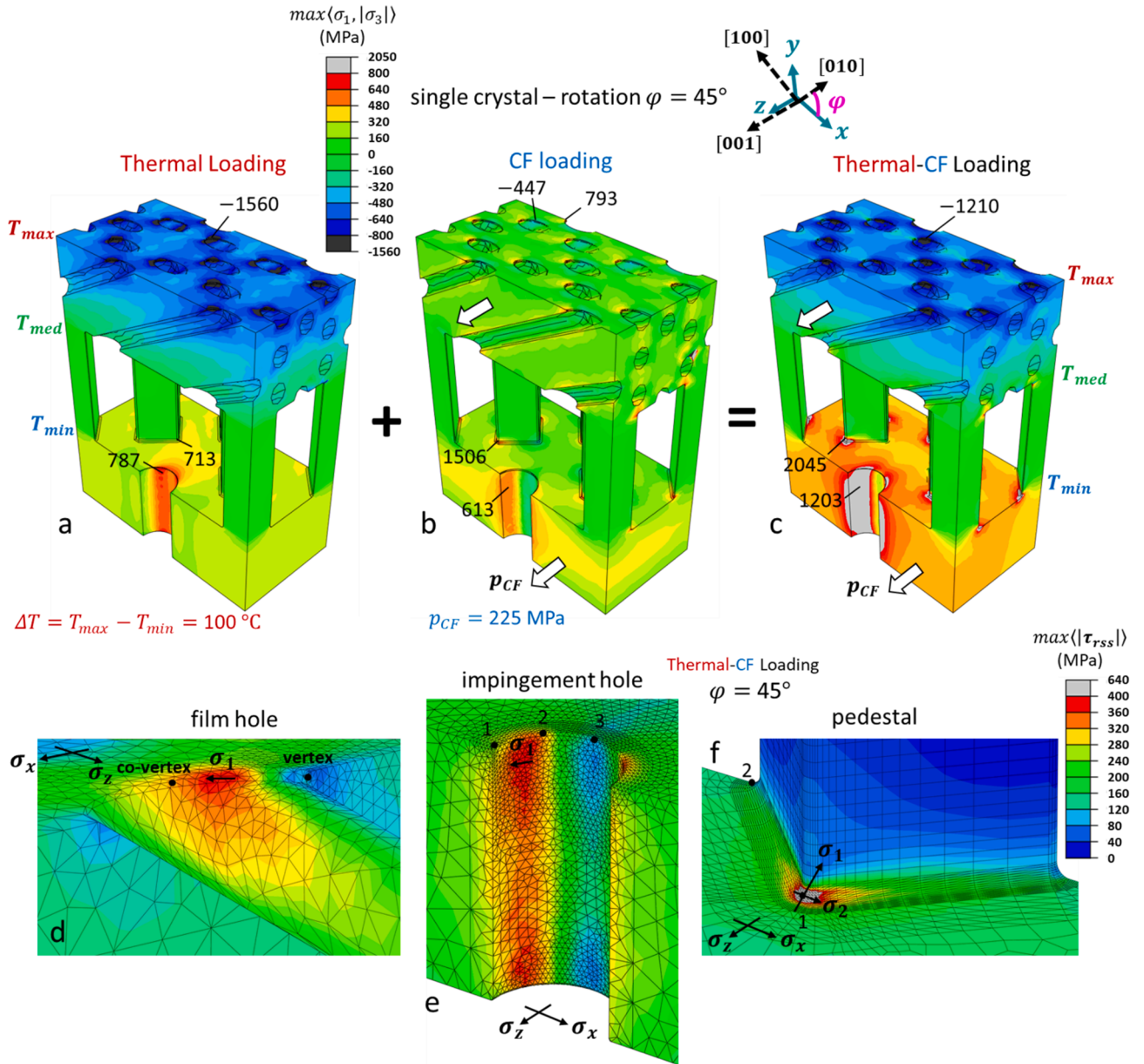


**Fig. 10.** Mechanical analysis results for the model in Fig. 1d with a crystal rotation of  $\varphi = 45^\circ$ . a) Stress field for pure thermal loading for the model in Fig. 1d with a crystal rotation of  $\varphi = 45^\circ$ . b) Stress field for pure centrifugal loading. c) Stress field for combined loading. d) Stresses at the outer rim of the film hole for combined loading. e) Stresses at the impingement hole for combined loading. f) Stresses at the inner pedestal fillet for combined loading. In a-c the absolute max principal stress is plotted, whereas in d-f the max absolute resolved shear stress is plotted.

$$\text{impingement hole: } \sigma_1 = \max(\sigma_{cx}, \sigma_{cz}) \bullet SCF_{imp}(4b)$$

$$\text{pedestal: } \sigma_1 = \sigma_{cz} \bullet SCF_{ped}(4c)$$

where  $\sigma_{cx}, \sigma_{cz}$  are the nominal cool wall stresses and  $\sigma_{hx}(y = -t_h/2)$  is the nominal stress at the outer surface of the hot wall (all determined theoretically in Section 4.3) and  $SCF$  represents the stress concentration factor, which is determined from the FE simulations and is plotted in Fig. 11. Each term in Eqs 4a-c accounts for global effects that apply to both single crystals and polycrystals, as well as anisotropic effects that apply only for a single crystal and scale with the Zener factor,  $A$ . The global effects related to the nominal stresses are:

- a) The  $\sigma_z/\sigma_x$  ratio increases with  $p_{CF}/\sigma_T$  in the cool wall and decreases in the hot wall ( $\sigma_x$  is independent of  $p_{CF}/\sigma_T$ ).
- b) A lower  $t_c/t_h$  ratio reduces both  $|\sigma_x|$  and  $|\sigma_z|$  in the hot wall at the cost of increasing the corresponding nominal stresses in the cool wall; this

explains the effect observed in all the Fig. 11a1-c1 and 11a2-c2 described in A.

The anisotropic effect for the nominal stresses is that the rotation,  $\varphi$ , decreases  $\sigma_z/\sigma_x$  in both walls by increasing  $|\sigma_x|$ ; this is because  $\sigma_x$  aligns with the compliant  $\langle 100 \rangle$  direction for  $\varphi = 0^\circ$  and with the stiff  $\langle 110 \rangle$  direction for  $\varphi = 45^\circ$ , whereas  $|\sigma_z|$  here always aligns with  $\langle 100 \rangle$ . The increase of  $|\sigma_x|$  is the major contributor to the effect observed in Fig. 11a1-b1 and Fig. 11a2-b2 described in B with regards to hole stresses.

The global effects related to  $SCF$  that are insensitive to the degree of anisotropy are:

- D) For an equibiaxial stress field, i.e.  $\sigma_z/\sigma_x = 1$ , the  $SCF$  is maximum at the vertex of the elliptical rim of the film hole in the  $x-z$  plane

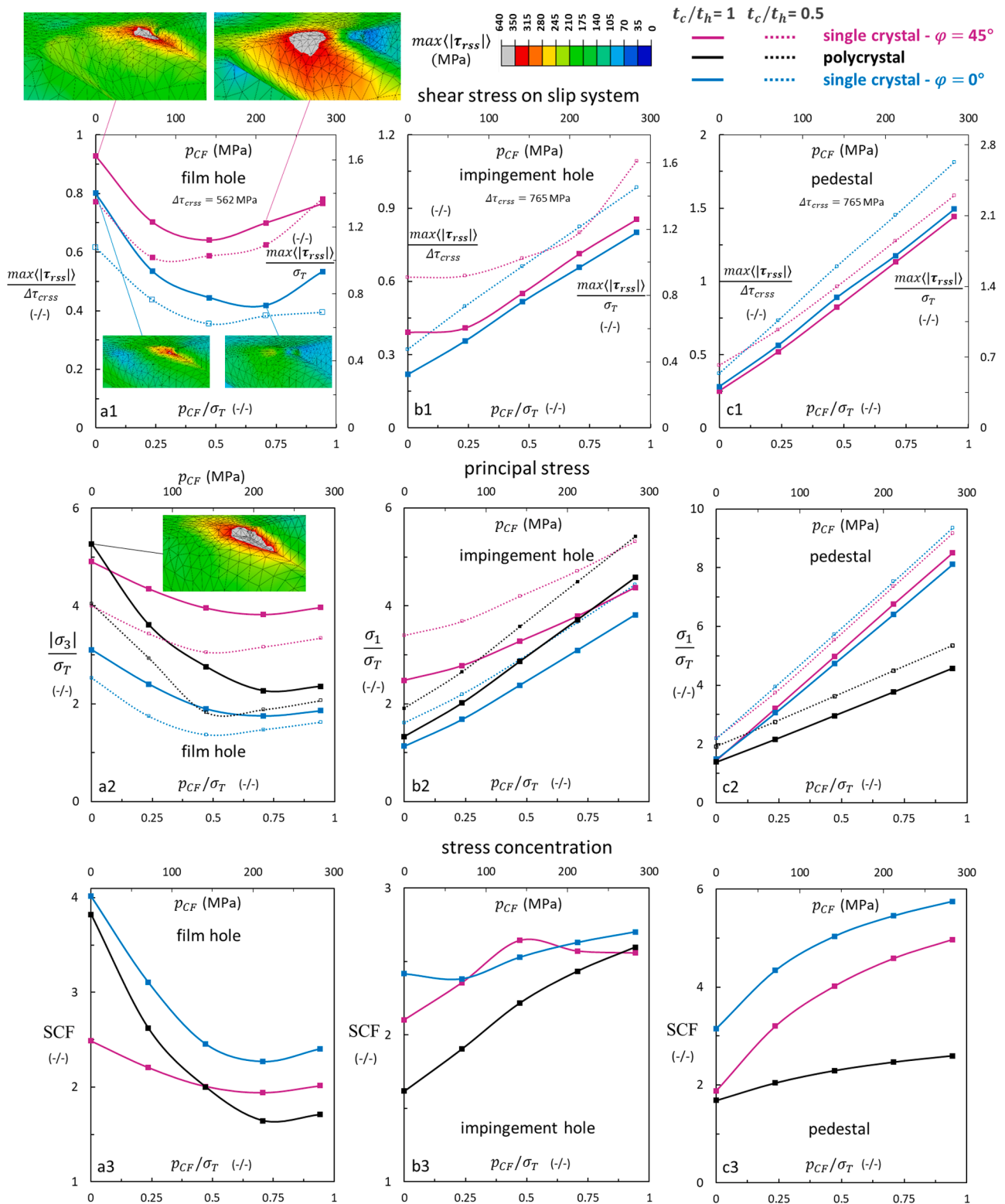


**Fig. 11.** Variation of stress quantities (vertical axes) with respect to centrifugal stress  $p_{CF}$  and centrifugal thermal loading ratio,  $p_{CF}/\sigma_T$  (two horizontal axes on each graph); two wall thickness ratios,  $t_c/t_h$ , and two single crystal orientation angles,  $\varphi$ , are considered, along with the case of a polycrystal. In a1-c1 the normalised values of max absolute resolved shear stress (RSS) are plotted for critical locations at the film hole, impingement hole and pedestal. For the same critical locations, a2-c2 plot the normalised values of the principal stress with max magnitude,  $|\sigma_3|$  or  $\sigma_1$ , whereas a3-c3 plot the stress concentration factor (SCF) as defined by Eqs 4a-c.

(Fig. 10d) and minimum at the co-vertex, whereas SCF is uniform along the circular rim of the impingement hole.

II) The increase of  $\sigma_z/\sigma_x$  in the cool wall due to increasing  $p_{CF}/\sigma_T$ , increases the maximum SCF at the pedestal filleted corner (see

Fig. 11c3) and the impingement hole (see Fig. 11b3) at which the critical location moves to point 1 shown in Fig. 10e; this explains the effect observed in Fig. 11b1-c1 and 11b2-c2 described in C with regards to the impingement hole and pedestal. In contrast,

the decrease of  $\sigma_z/\sigma_x$  with increasing  $p_{CF}/\sigma_T$  in the hot wall reduces the SCF at the vertex of the film hole and increases the SCF at the co-vertex, i.e. the location of the maximum SCF departs from the vertex and moves towards the co-vertex (see contours attached in Fig. 11a1); this results in a large reduction of the SCF at the critical location as  $p_{CF}/\sigma_T$  increases (see Fig. 11a3), followed by an increase of SCF at large  $p_{CF}/\sigma_T$  values. This phenomenon explains the effect observed in Fig. 11a1 and 11a2 with regards to the film hole described in C.

The anisotropic effect with regards to the SCF is that the SCF increases at locations where the principal stress direction aligns with secondary crystallographic directions. For example, when  $\varphi = 0^\circ$  the  $\sigma_1$  stress along the impingement hole circumference aligns with the  $\langle 100 \rangle$  crystal axes at points 1, 3 and with  $\langle 110 \rangle$  (the stiffest direction) at point 2 (see Fig. 10e); as a result for  $p_{CF}/\sigma_T = 0$  the maximum SCF occurs at point 2 and is higher than the SCF corresponding to a polycrystal material (shown in Fig. 11b3), by a degree which depends on the Zener factor,  $A$ . When,  $\varphi = 45^\circ$ ,  $\sigma_1$  aligns with  $\langle 100 \rangle$  at point 1, with  $\langle 110 \rangle$  at point 3 and with  $\langle 111 \rangle$  at point 2 (points denoted in Fig. 10e); therefore the maximum SCF occurs again at point 2, followed by a lower value at a point 3 and an even lower one at point 1. The same effects apply at the film hole with the difference here being that, due to the ellipticity and inclination, the location of the maximum SCF tends to be near the vertex; nevertheless, we generally find that even when  $\varphi = 0^\circ$  and  $p_{CF}/\sigma_T = 0$ , the higher stiffness along  $\langle 110 \rangle$  causes the location of the maximum SCF to slightly depart from the vertex, where it occurs for a polycrystal (compare contours between Fig. 11a1 and Fig. 11a2). Regarding the pedestal, the  $\sigma_1$  stress in Fig. 10f aligns with  $\langle 110 \rangle$  and  $\langle 111 \rangle$  for  $\varphi = 0^\circ$  and  $\varphi = 45^\circ$ , respectively; despite this, the SCF in Fig. 11c3 is lower for  $\varphi = 45^\circ$ , which is attributed to the significantly lower value of  $\sigma_z/\sigma_x$  [2].

## 5. Evaluation of results

We now evaluate all our results and discuss their significance. A key highlight is that a DWTC system with large outer wall porosity (large film hole density) provides a high cooling effectiveness at moderate mass flow rates, allowing for theoretical transpiration cooling to be approached. In particular, a high porosity enhances convective cooling along the film hole surfaces, gives the component effective cooling near the external surface and reduces the temperature difference between the outer and inner wall. The outer wall porosity of 19.2 % in the geometry analysed here (Fig. 2a1) leads to total thermal differences across the two walls in the range 190–130 °C, which is a significant advancement when compared to values of  $\sim 270$  °C reported previously [2] for a system with an outer wall porosity of 10 % (Fig. 2a2). By also considering that thermal stresses are driven by these thermal differences and that the presence of film holes reduces the apparent elastic stiffness of the outer wall, we can argue that a high porosity simultaneously offers substantial improvements in mechanical performance. However, there remain aspects requiring further consideration, such as the impact of film hole density and coolant mass flow rate on aerodynamic penalty [29] and engine efficiency [12,30] and potential fatigue cracking events due to crystallographic slip caused by narrow spacing between film holes [31,32]. Contrary to these former reports, the current study shows that a close proximity of film holes does not cause elevated shear stresses at the ligament sections between holes, which may be due to the fact that previous papers only considered transverse film holes and uniform uniaxial loading. Despite our results encouraging the use of high film hole density, they only account for an elastic material response, suggesting that further validation is required in the elasto-plastic-creep regime. This will be explored more fully in a future publication.

We should recognise here that the above structural performance benefits of high outer wall porosity are considered to arise by the reduction of thermal stresses alone, on the basis that in double wall

blades these stresses dominate over mechanical stresses induced by centrifugal and/or aerodynamic loading [2,22]. However, based on the current film hole arrangement, when the outer wall porosity is as high as 19.2 % (Fig. 2a1) the nominal centrifugal stress can increase by a factor of 2.73 due to a drastic reduction in the net cross section of the walls in the streamwise direction of the blade (explained in Appendix D); the factor reduces to only 1.45 for a porosity of 10 % (Fig. 2a2). Thus, for an engine operating at 12000 rpm and for the geometric parameters of Table 1, we predict (using the scheme in Appendix D) that the root of the blade will experience a nominal centrifugal stress of 310 MPa with a net-section stress of 847 MPa for 19.2 % porosity (Fig. 2a1) and a net-section stress of only 450 MPa for 10 % porosity (Fig. 2a2). These values can be overly conservative, in that traditional blade designs involve an increasing wall thickness towards the blade root [33], but concerns arise regarding the integrity of the high porosity system at high engine speeds. Locally, fatigue is a major concern since the net stress will be scaled further by a large stress concentration factor at the hole and pedestal features. Globally, high mechanical stresses can activate ratchetting mechanisms (incremental plastic collapse of the whole structure within a small number of cycles), especially for the out-of-phase thermo-mechanical cycling typically experienced in turbine blades [34]. Another potential global failure mechanism is the continuous accumulation of tensile creep deformation during the high temperature stage of each loading cycle. All the above suggest that high outer wall porosity systems can drastically reduce thermal stresses but at the detriment of elevated mechanical stresses which can give rise to additional failure modes in addition to fatigue. These mechanical stresses, however, can be mitigated by using alternative film hole arrangements that reduce the net wall section in the streamwise direction.

An additional characteristic of the high outer wall porosity DWTC system considered here is that the impingement jet becomes a secondary cooling mechanism, providing the system with redundancies. As an example, particle blockage may be induced by volcanic ash [35] or dust [36] reducing the film effectiveness as well as internal convective cooling of an individual film hole. However, this could be partially compensated by nearby film holes which will have a greater share of mass flow, elevating their contribution to film and convective cooling. Furthermore, any increase in metal temperatures may be limited by the impingement jet and other internal surfaces, i.e. pedestals. These features become increasingly important as small film hole diameters have increased susceptibility to blockage from external deposition. Further research should look to understand the likelihood of blockage and how impactful such events would be.

In terms of internal cooling features, a key highlight of our results is that despite a reduction of wall spacing/pedestal height promotes impingement cooling and reduces the outer-inner wall thermal difference at low coolant flow rates, it has a negative influence on the coolant flow distribution to the film holes and significantly enhances the risk of hot gas ingestion. This must be avoided as the internal surfaces would not be protected by a thermal barrier coating and therefore would be susceptible to oxidation and thermal fatigue. It is also worth considering that in this study a constant external pressure was applied to the outlets, whereas in reality a pressure gradient would be present on the external blade surface. A positive pressure gradient from leading to trailing film hole will further reduce the mass flow to the leading film holes and is likely to exasperate the poor flow distribution. Consequently, we argue that the reduction of outer-inner wall thermal difference associated with short pedestals is outweighed by the risk of hot-gas ingestion, and thus the pedestals should generally be of sufficient length in practice to prevent ingestion. Future research may look into identifying the minimum wall spacing/pedestal height for which hot-gas ingestion is avoided, given a film hole arrangement.

It is emphasised here again that given a temperature field the pedestal height does not influence thermal stresses, as explained in [15] based on the kinematics of a turbine blade; it can only influence aerodynamic bending stresses but these are much smaller than thermal

stresses, particularly in double wall turbine blades [2]. This implies that from a mechanical point of view, pedestal height is a secondary design variable. The wall thickness ratio, on the other hand, has a drastic influence on the thermal stress field and is the most significant design variable when it comes to structural integrity, along with the geometry of the film holes (inclination, shape). Our results show that varying the inner wall thickness for a constant outer wall thickness has a small influence on the aerothermal field, suggesting that designers can consider this to be a flexible constraint. Our results for an anisotropic material are consistent with previous recommendations based on isotropic materials, in that the inner wall thickness should be minimised to reduce thermal stresses at the film holes where the largest potential for fatigue cracking is displayed [14]. It is important, nevertheless, to determine the lower threshold for such a reduction given the inevitable increase of tensile thermal stresses at the impingement hole and pedestal fillet. In particular, we have shown here that a low inner wall thickness combined with severe centrifugal loading (along with thermal loading) can lead to severe tensile stresses and therefore reverse plasticity in a pedestal with a very sharp fillet (radius 30  $\mu\text{m}$ ); however, this represents an extreme stress concentration case and is deliberately used here in order to study the implications of poor manufacturing. In practise, a larger fillet radius is expected to result in a drastically lower stress concentration [15], giving enough room for reducing the inner wall thickness for the purpose of improving the fatigue performance at the film holes. An elasto-plastic-creep FE analysis will help verify this argument.

We have not explored film hole geometry effects in this study, but we have identified an important anisotropic effect of relevance to the relation between hole shape and fatigue. We have shown that the critical stress at the vicinity of a hole has the tendency to occur at the location where the principal stress direction aligns with the stiffest crystallographic direction. As a result, the critical location for fatigue changes significantly depending on the biaxial wall nominal stress ratio, i.e. the thermal-centrifugal load combination, especially along a non-circular hole rim, e.g. the elliptical rim of the currently used film holes. This makes it difficult for a designer to know the exact critical location without performing FE analysis for the particular loading combination of interest. In a previous study [37] we recommended reducing the degree of ellipticity of the film hole rim (the intersection between an inclined cylinder and the plane of the wall) in order to reduce stress concentration at the vertex (at the cost of increasing stress concentration at the co-vertex); however, this concerned pure thermal loading and isotropic elasticity where the critical fatigue location always lies at the elliptical vertex. In practise, the new results here suggest that ellipticity should not be reduced in cases of high centrifugal loading because the highest stresses occur at the elliptical co-vertex rather than the vertex. This implies that the optimal film hole shape may vary along the length of the turbine blade, i.e. between a circular rim near the blade tip (zero centrifugal stresses) and an increasingly elliptical rim towards the blade root (maximum centrifugal stresses). It should be acknowledged, however, that modifying the film hole shape for optimal fatigue performance will generally require considerations not only of the elastic anisotropy but also the creep-plastic anisotropy of the material [38].

All the above suggest that a useful general practise may be followed for the design of turbomachinery components with cooling holes. This methodology involves CFD-heat transfer analysis in a repeating unit cell of the component to explore the aerothermal performance and to generate a temperature field that can then be applied in elastic FE analysis of the unit cell. An initial hole shape optimisation for the specific in-service thermal-centrifugal stress conditions can then be performed in the elastic range. Finally, the 'almost optimised' hole shape geometry can be used in simplified hole-plate FE models (typically reduced in mesh size due to high computational cost of crystal plasticity analysis) to simulate the local creep-plasticity behaviour under cyclic thermomechanical loading, with the ultimate aim to fully optimise the

design.

## 6. Conclusions

In this paper a computational methodology for the aerothermal and mechanical design of double wall transpiration cooled (DWTC) systems for gas turbine blades and a range of high temperature thin walled components has been presented.

We find that systems of high film hole density (high wall porosity) result in a better cooling efficiency and thermal stress performance compared to previously studied DWTC systems of modest outer wall porosity. However, depending on the film hole arrangement they can result in an elevation of mechanical stresses arising from centrifugal loading due to a reduction in the net wall section. In particular, cooling effectiveness values of over 0.8 were observed on the external hot surface and in some places theoretical transpiration was achieved. Such systems represent a clear advance in the development of efficient cooling systems for turbine blades, although further research on blockage, pressure margin and flow migration are required.

In terms of geometric effects, we find that connecting the two walls with short pedestals enhances the internal impingement cooling but at a higher risk of hot gas ingestion; it is therefore suggested that the pedestals should be short, but long enough to avoid such effects. The inner wall thickness, on the other hand, is shown to have less impact on the aerothermal response, giving designers the freedom to reduce inner wall thickness for the scope of reducing thermal stresses in the more critical outer wall, thus improving the mechanical performance at the film holes.

The stress concentration at the film hole, impingement hole and pedestal fillets is influenced by several effects that can either be termed global and independent of the anisotropic properties of the material or depend on the anisotropic nature of the material response. Anisotropy increases significantly the difficulty in predicting the critical hot spot stress location at the film holes, adding complexity to the task of optimising film hole shape for optimal fatigue performance. Crystal orientation is shown to have little influence on pedestal stresses as opposed to impingement hole stresses and especially film hole stresses, which show a strong influence. Despite the principal axis of single crystal gas turbine blades being in alignment with the compliant  $\langle 100 \rangle$  crystallographic direction, it is highlighted that local stresses at features, e.g. holes and pedestals, will inevitably occur along the stiffer, secondary crystallographic directions, e.g.  $\langle 110 \rangle$  and  $\langle 111 \rangle$ .

The methodology and results presented in this paper aim to facilitate the implementation of the DWTC technology in turbomachinery and other high temperature applications.

## Declaration of Competing Interest

The authors declare the following financial interests/personal relationships which may be considered as potential competing interests: [Prof Peter Ireland reports financial support was provided by Engineering and Physical Sciences Research Council].

## Data availability

Data will be made available on request.

## Acknowledgements

The work was supported by EPSRC programme grant EP/P000878/1, with further support from Rolls-Royce PLC. Dr Alex Murray is acknowledged for useful discussions on the aerothermal aspects and Dr Nicolo Grilli for useful discussions on crystal anisotropy.



## Appendix A. . Details on aerothermal analysis steps - section 2.1

### A1. Internal CFD analysis

The important outputs of the CFD analysis are the coolant velocity,  $v_f$ , and temperature at each film hole exit,  $T_{f,outlet}$ . An unstructured mesh is used with fifteen prism layers along fluid–solid interfaces with an overall height of 0.1 mm and a growth rate of 1.2, to keep the non-dimensional wall height,  $y^+ \leq 1$ . The solver is pressure-based and uses the realizable  $k - \epsilon$  turbulence model, with enhanced wall function and thermal effects enabled. Air is treated as an ideal gas for the fluid domain with thermal conductivity and viscosity evaluated by kinetic theory and the Sutherland method, respectively. The role of radiative heat flux has not been considered in the present study, since the emphasis here is placed on understanding the role of internal features on the aerothermal and mechanical performance based on a fixed heat load. We can therefore reasonably assume here that the magnitude of the heat load i.e. whshapeether radiation heat flux is combined with convective heat flux, will not alter our conclusions. It can be also noted that in the study by Li et al. [43], the radiative error, i.e. the ratio of external radiative heat flux compared to the total heat flux applied onto the hot wall ( $q_{rad} / q_{tot}$ ) for pure air was between 5 and 10 % for a temperature ratio,  $T_\infty/T_c$ , in the range 1.75 – 2; in this study  $T_\infty/T_c = 1.8$  and therefore the error can be assumed to be small.

### A2. Modified Goldstein-Sellers method

Goldstein's [39] empirical formulation of film effectiveness,  $\eta_{fi}^-$ , concerns a single film jet and provides the shape and strength of heat protection as a function of the blowing ratio,  $M$ , i.e.  $\eta_{fi}^- = \eta_{fi}^-(M, \xi, \zeta)$  where  $\xi, \zeta$  are streamwise and spanwise positions with respect to the film hole. Firstly, the coolant exit velocity at each hole,  $v_f$  (provided by CFD) and the blowing ratio,  $M$  are passed into the modified Goldstein equation [39]:

$$\eta_{fi}^-(M, \xi, \zeta) = \frac{M v_{film} D_{film}}{8 \alpha_t \left( \frac{\xi}{D_{film}} + \xi_{decay} \right)} \exp \left[ - \left( \frac{\zeta}{c_1} \right)^{c_2} \right]$$

The turbulent diffusivity  $\alpha_t$  and variable  $\xi_{decay}$  are dependent on  $M$ , and values for these are based on experimental and correlation data (see Murray et al. [6], Baldauf et al. [40]). The referenced studies were also used to find the variables influencing the spanwise decay and shape,  $c_1$  and  $c_2$ , which are dependent on  $M, \xi$ . The coolant temperature at the film hole exit,  $T_{f,outlet}$  (provided by CFD) along with  $\eta_{fi}^-(M, \xi, \zeta)$  are then used in:

$$\eta_{f,i}(\xi, \zeta) = \eta_{fi}^-(M, \xi, \zeta) \frac{T_\infty - T_{f,outlet}}{T_\infty - T_c}$$

The film effectiveness in an array of cooling holes where interactions of film jets come into play is then found by Sellers' superposition equation [41]:

$$\eta_f(x, y) = 1 - \prod_{i=1}^n (1 - \eta_{f,i}(x, y))$$

where the local positions  $\xi, \zeta$  are transformed into global positions  $x, y$ . The adiabatic temperature field is finally determined by:

$$\eta_f(x, y) = \frac{T_\infty - T_{aw}(x, y)}{T_\infty - T_c}$$

In this way the aerothermal field output from a repeating unit-cell can be extended to the enlarged domain shown in Fig. 2c.

### A3. FE heat transfer analysis

The full domain uses seven repeating unit-cells attached to an upstream and downstream flange section and is solved in ANSYS Mechanical using results from the CFD as well as the empirically found film effectiveness. Wall temperatures and heat fluxes are exported from the unit-cell CFD to a Matlab program to determine the surface heat transfer coefficients,  $h$ , based upon wall temperature,  $T_w$ , inlet coolant temperature,  $T_c$ , and the wall heat flux,  $q$ , through the relation  $h = q/(T_w - T_c)$ . These values are extended from a single unit-cell to the unit-cell repeating area and exported as boundary conditions into ANSYS Mechanical alongside  $T_{aw}$  and  $h$  for the hot-side surface calculated by the film effectiveness methodology. The film effectiveness applied here is assumed to be the middle cell of three unit-cells in the spanwise direction. As such, the film superposition has lateral influence from adjacent unit-cells. The upstream and downstream plate extents are assumed to be perfectly insulated. Internal walls outside the repeating blocks are given the area-average of the CFD results for that component feature. As an example, the pedestals would take the area-averaged heat transfer coefficient observed in the unit-cell as calculated by  $h = q/(T_w - T_c)$ . Finally, with all inputs provided, the FEA solver calculates the temperature field for all solid surfaces throughout the domain.

This method represents a numerically efficient scheme for solving complex internal cooling geometries, but the fluid and solid domains are inherently decoupled. This occurs in two ways, firstly the films are not modelled in the CFD and therefore there is no external cooling effect. Secondly, in the FEA the internal fluid and wall temperatures are decoupled. In the first instance the film effectiveness is underestimated as  $T_f$  will be higher from the unit-cell CFD than if films were applied. In the second instance the internal heat transfer will have an associated error given that in the FEA the film effectiveness is applied but not in the unit-cell domain. Although the flow field is not likely to be significantly altered due to changes in wall temperature and therefore the calculated heat transfer coefficients should be representative. These differences were studied in [47] where it was highlighted that in situations with high film effectiveness an underprediction of the cooling effectiveness occurs, compared to a fully coupled methodology.

## Appendix B. . Transformation from crystal system to global system - section 4.3

The relationships between the three elastic moduli and three compliance constants are:

$$S_{11} = \frac{C_{11} + C_{12}}{(C_{11} - C_{12})(C_{11} + 2C_{12})}, S_{12} = -\frac{C_{12}}{(C_{11} - C_{12})(C_{11} + 2C_{12})}, S_{44} = \frac{1}{C_{44}} \quad (B1)$$

The compliance matrix is:

$$S = \begin{bmatrix} S_{11} & S_{12} & S_{12} & 0 & 0 & 0 \\ S_{12} & S_{11} & S_{12} & 0 & 0 & 0 \\ S_{12} & S_{12} & S_{11} & 0 & 0 & 0 \\ 0 & 0 & 0 & S_{44} & 0 & 0 \\ 0 & 0 & 0 & 0 & S_{44} & 0 \\ 0 & 0 & 0 & 0 & 0 & S_{44} \end{bmatrix} \quad (B2)$$

The transformation from the crystal system to the blade system based on the sequence of  $\varphi$ ,  $\theta$ ,  $\psi$  rotations is given by the matrix:

$$T = \begin{bmatrix} \cos\varphi & -\sin\varphi & 0 \\ \sin\varphi & \cos\varphi & 0 \\ 0 & 0 & 1 \end{bmatrix} \bullet \begin{bmatrix} 1 & 0 & 0 \\ 0 & \cos\theta & -\sin\theta \\ 0 & \sin\theta & \cos\theta \end{bmatrix} \bullet \begin{bmatrix} \cos\psi & -\sin\psi & 0 \\ \sin\psi & \cos\psi & 0 \\ 0 & 0 & 1 \end{bmatrix} \quad (B3)$$

For column vector operations,  $T$  must be expanded into:

$$\bar{T} = \begin{bmatrix} T_{11}^2 & T_{12}^2 & T_{13}^2 & 2T_{12}T_{13} & 2T_{11}T_{13} & 2T_{11}T_{12} \\ T_{21}^2 & T_{22}^2 & T_{23}^2 & 2T_{22}T_{23} & 2T_{21}T_{23} & 2T_{21}T_{22} \\ T_{31}^2 & T_{32}^2 & T_{33}^2 & 2T_{32}T_{33} & 2T_{31}T_{33} & 2T_{31}T_{32} \\ T_{21}T_{31} & T_{22}T_{32} & T_{23}T_{33} & T_{22}T_{33} + T_{23}T_{32} & T_{21}T_{33} + T_{23}T_{31} & T_{21}T_{32} + T_{22}T_{31} \\ T_{11}T_{31} & T_{12}T_{32} & T_{13}T_{33} & T_{12}T_{33} + T_{13}T_{32} & T_{11}T_{33} + T_{13}T_{31} & T_{11}T_{32} + T_{12}T_{31} \\ T_{11}T_{21} & T_{12}T_{22} & T_{13}T_{23} & T_{12}T_{23} + T_{13}T_{22} & T_{11}T_{23} + T_{13}T_{21} & T_{11}T_{22} + T_{12}T_{21} \end{bmatrix} \quad (B4)$$

where  $T_{ij}$  are the components of  $T$  computed from Eq B3.

#### Appendix C. . Volume averaged elastic properties for a polycrystal - section 4.1

Voigt proposed that the shear modulus of a polycrystalline material can be found by averaging the stress expressions for a given strain over all possible directions in a single crystal, whereas Reuss proposed that the relations expressing strain for a given stress should be averaged, giving the following results:

$$\bar{G}_{Voigt} = \frac{C_{11} - C_{12} + 3C_{44}}{5} \quad (C1)$$

$$\bar{G}_{Reuss} = \frac{5C_{44}(C_{11} - C_{12})}{4C_{44} + 3(C_{11} - C_{12})} \quad (C2)$$

where  $\bar{G}_{Voigt}$  and  $\bar{G}_{Reuss}$  overpredict and underpredict the true shear modulus as they assume uniform strain and uniform stress through the polycrystal, respectively. Hill showed that the reality lies between the above extremes, such that the true modulus is very closely approximated by the average,  $\bar{G}_{Hill} = (\bar{G}_{Voigt} + \bar{G}_{Reuss})/2$ . By using  $\bar{G}_{Hill}$  and the Bulk modulus,  $B = (C_{11} + 2C_{12})/3$ , the volume averaged Poisson's ratio and Young's modulus are then computed by:

$$\bar{\nu} = \frac{3B - 2\bar{G}_{Hill}}{2(3B + \bar{G}_{Hill})} \quad (C3)$$

$$\bar{E} = 2G(1 + \bar{\nu}) \quad (C4)$$

#### Appendix D. . Calculation of net centrifugal stress $p_{CFnet}$ – Section 3.4

We adopt the calculation scheme previously described in [2]. This involves an initial calculation of the centrifugal (CF) stress,  $p_{CF} = (\rho + \rho^*)\omega^2\tilde{L}_x$ , carried by the gross cross section of the walls, where  $\rho$  is the material density (kg/m<sup>3</sup>),  $\omega$  is the turbine rotational speed (rad/s) and  $\tilde{L}_x = L_x(R_{tip} - 0.5L_x)$  is a function of the distance,  $L_x$  (mm), between the blade tip and the blade location of interest as well as the distance,  $R_{tip}$  (mm), between the blade tip and the engine axis;  $\rho^*$  (kg/m<sup>3</sup>) is an 'equivalent' density determined by  $\rho^*\omega^2\tilde{L}_x = (F_{ped} - F_{holes})/S$ , which can increase or decrease  $p_{CF}$  (MPa) depending on whether the centrifugal (CF) force added by the total inertia of pedestals,  $F_{ped}$ , (from the blade tip to the blade location of interest) is larger or smaller than the CF force deduced by the total volume of holes,  $F_{holes}$  (from the blade tip to the blade location of interest);  $S = s(t_h + t_c)$  denotes the gross section of the walls (mm<sup>2</sup>) for a unit cell length,  $s$  (mm), along the x axis (Fig. 1d). In Fig. 1d there exist four planes where pedestals are repeated (pedestal centreline distance along z axis is here equal to the unit cell width  $w$ ) and one plane where pedestals are repeated every  $2w$  in order to accommodate the impingement hole. This gives [2]:

$$F_{ped} = \rho\omega^2V_{ped} \left\{ 4 \frac{L_x}{w} [R_{tip} + 0.5(w - L_x)] + \frac{L_x}{2w} [R_{tip} + 0.5(2w - L_x)] \right\} \quad (D1)$$

Impingement holes are repeated every  $2w$  in a single plane of Fig. 1d, whereas an equivalent of four film holes is repeated every  $w$ , and another four film holes every  $0.5w$ , giving [2]:

$$F_{\text{holes}} = \rho \omega^2 V_{\text{imp}} \frac{L_x}{2w} [R_{\text{tip}} + 0.5(2w - L_x)] + 4\rho \omega^2 V_{\text{film}} \left\{ \frac{L_x}{w} [R_{\text{tip}} + 0.5(w - L_x)] + \frac{L_x}{0.5w} [R_{\text{tip}} + 0.5(0.5w - L_x)] \right\} \quad (D2)$$

Pedestal, impingement hole and film hole volumes are respectively given by  $V_{\text{ped}} = HD_{\text{ped}}^2$ ,  $V_{\text{imp}} = 0.25\pi t_c D_{\text{imp}}^2$  and  $V_{\text{film}} = 0.25\pi t_h D_{\text{film}}^2 / \cos^2 \gamma$  ( $\gamma = \pi/3$  rad). The cross sections removed by the presence of impingement and film holes at the  $\bar{z} = 1$  plane are  $S_{\text{imp}} = D_{\text{imp}} t_c$  and  $S_{\text{film}} = D_{\text{film}} t_h / \cos^2 \gamma$ , such that the net centrifugal stress applied as a boundary where load is prescribed in the FE model is  $p_{\text{CFnet}} = p_{\text{CF}} S / (S - S_{\text{imp}} - 2S_{\text{film}})$ . Note that there exist two planes in Fig. 1d in which a section equivalent to four film holes is removed, such that the maximum net stress is  $p_{\text{CFnetMax}} = p_{\text{CF}} S / (S - S_{\text{imp}} - 4S_{\text{film}})$ . If  $F_{\text{walls}} = \rho \omega^2 \tilde{L}_x S$  is the CF force associated with the inertia of the walls, then for Fig. 1d (or Fig. 2a1) and the dimensions given in Table 1 we get  $F_{\text{ped}} / F_{\text{walls}} \approx 0.22$  and  $F_{\text{holes}} / F_{\text{ped}} \approx 0.92$ , implying that the total inertia of pedestals acts to increase  $p_{\text{CF}}$  by 22 % but due to the high density of film holes 92 % of this increase is cancelled. In contrast, the system studied previously in [2] and shown here in Fig. 2a2 ( $D_{\text{film}} = D_{\text{imp}} = D_{\text{ped}} = t_h = t_c = 1$  mm,  $s = 8$  mm,  $w = 4$  mm) corresponds to  $F_{\text{ped}} / F_{\text{walls}} \approx 0.048$  and  $F_{\text{holes}} / F_{\text{ped}} \approx 0.72$ . The key difference is that the system in Fig. 2a2 gives  $p_{\text{CFnetMax}} = p_{\text{CFnet}} = 1.45 p_{\text{CF}}$  whereas Fig. 2a1 gives  $p_{\text{CFnetMax}} = 2.73 p_{\text{CF}}$ .

#### Appendix E. . Calculation of material yield stress range $\Delta\tau_{\text{crss}}$ – Section 4.4

We consider the monotonic stress–strain experimental data obtained by Allan for CMSX-4 [42] for a macroscopic strain rate of  $10^{-4}$ /s. We assume here that plasticity is driven only by the 12 octahedral slip systems  $\{111\}\langle 110 \rangle$  and that the yield strength is rate independent and pressure independent i.e. equal between tension and compression. Given that the Schmid factor associated with  $\{111\}\langle 110 \rangle$  slip is small for macroscopic loading along the  $\langle 111 \rangle$  direction and that in most cases stresses at holes and pedestals occur near the  $\langle 110 \rangle$  direction, we calculate the critical resolved shear stress range,  $\Delta\tau_{\text{crss}}$ , based on the macroscopic yield stress data for  $\langle 110 \rangle$  oriented crystals [42]. By taking the average data between compression and tension, the room temperature yield strength used here is  $\sigma_{y(110)} = 1100$  MPa; multiplying by the Schmid factor of 0.4082 gives the room temperature critical resolved shear stress,  $\tau_{\text{crss0}} = 450$  MPa. The strength decreases to  $\sigma_{y(110)} = 700$  MPa at  $1000^\circ\text{C}$  and  $\sigma_{y(110)} = 440$  MPa at  $1100^\circ\text{C}$ , which respectively correspond to the temperatures at the internal features (impingement hole and inner pedestal fillet) and external features (film hole) at full loading; this implies critical resolved shear stresses of  $\tau_{\text{crssT}} = 286$  MPa and  $\tau_{\text{crssT}} = 180$  MPa at internal and external features at high temperature and yield stress ranges of  $\Delta\tau_{\text{crss}} = 736$  MPa and  $\Delta\tau_{\text{crss}} = 630$  MPa, respectively.

#### References

- [1] A.V. Murray, P.T. Ireland, E. Romero, Experimental and Computational Methods for the Evaluation of Double-Wall, Effusion Cooling Systems, *J. Turbomach.* 142 (11) (2020).
- [2] C. Skamniotis, M. Courtis, A.C. Cocks, Multiscale analysis of thermomechanical stresses in double wall transpiration cooling systems for gas turbine blades, *Int. J. Mech. Sci.* 207 (2021) 106657.
- [3] A. Epishin, et al., Investigation of Elastic Properties of the Single-Crystal Nickel-Base Superalloy CMSX-4 in the Temperature Interval between Room Temperature and  $1300^\circ\text{C}$ , *Crystals* 11 (2) (2021) 152.
- [4] Dye, D., et al. Welding of Single Crystal Superalloy CMSX-4: Experiments and Modeling. in *Superalloys 2004* (Tenth International Symposium). 2004.
- [5] Reed, R.C., *The superalloys: fundamentals and applications*. 2008: Cambridge university press.
- [6] A.V. Murray, et al., High Resolution Experimental and Computational Methods for Modelling Multiple Row Effusion Cooling Performance, *International Journal of Turbomachinery, Propulsion and Power* 3 (1) (2018) 4.
- [7] M. Kim, et al., Experimental investigation of effusion and transpiration air cooling for single turbine blade, *Appl. Therm. Eng.* 182 (2021) 116156.
- [8] R. Krewinkel, A review of gas turbine effusion cooling studies, *Int. J. Heat Mass Transf.* 66 (2013) 706–722.
- [9] M. Courtis, et al., Influence of Spanwise and Streamwise Film Hole Spacing on Adiabatic Film Effectiveness for Effusion-Cooled Gas Turbine Blades, *International Journal of Turbomachinery, Propulsion and Power* 6 (3) (2021) 37.
- [10] F. Satta, G. Tanda, Effect of discrete-hole arrangement on film-cooling effectiveness for the endwall of a turbine blade cascade, *Appl. Therm. Eng.* 91 (2015) 507–514.
- [11] W. Li, et al., On improving full-coverage effusion cooling efficiency by varying cooling arrangements and wall thickness in double wall cooling application, *J. Heat Transfer* 141 (4) (2019).
- [12] G.C. Ngetich, et al., A three-dimensional conjugate approach for analyzing a double-walled effusion-cooled turbine blade, *J. Turbomach.* 141 (1) (2019).
- [13] A. Wambersie, et al., Experiments of Transpiration Cooling Inspired Panel Cooling on a Turbine Blade Yielding Film Effectiveness Levels over 95%, *International Journal of Turbomachinery, Propulsion and Power* 6 (2) (2021) 16.
- [14] C.G. Skamniotis, A.C. Cocks, Creep-plasticity-fatigue calculations in the design of porous double layers for new transpiration cooling systems, *Int. J. Fatigue* (2021) 106304.
- [15] C.G. Skamniotis, A.C. Cocks, 2D and 3D thermoelastic phenomena in double wall transpiration cooling systems for gas turbine blades and hypersonic flight, *Aerosp. Sci. Technol.* (2021) 106610.
- [16] R. Kumar, et al., Thermo-mechanical analysis and estimation of turbine blade tip clearance of a small gas turbine engine under transient operating conditions, *Appl. Therm. Eng.* 179 (2020) 115700.
- [17] R. Mücke, O.-E. Bernhardt, A constitutive model for anisotropic materials based on Neuber's rule, *Comput. Methods Appl. Mech. Eng.* 192 (37–38) (2003) 4237–4255.
- [18] H. Zhou, et al., Crystal plasticity analysis of cylindrical holes and their effects on the deformation behavior of Ni-based single-crystal superalloys with different secondary orientations, *Int. J. Plast.* 119 (2019) 249–272.
- [19] V.S. Patil, R. Vedula, Local heat transfer for jet impingement onto a concave surface including injection nozzle length to diameter and curvature ratio effects, *Exp. Therm. Fluid Sci.* 92 (2018) 375–389.
- [20] S.V. Garimella, B. Nenaydykh, Nozzle-geometry effects in liquid jet impingement heat transfer, *Int. J. Heat Mass Transf.* 39 (14) (1996) 2915–2923.
- [21] E. Elmukashfi, et al., Analysis of the Thermomechanical Stresses in Double-Wall Effusion Cooled Systems, *J. Turbomach.* 142 (5) (2020).
- [22] C. Skamniotis, A.C. Cocks, Thermal and centrifugal stresses in curved double wall transpiration cooled components with temperature dependent thermoelastic properties, *Int. J. Solids Struct.* (2021) 111273.
- [23] C. Skamniotis, A.C. Cocks, Analytical shakedown, ratchetting and creep solutions for idealized twin-wall blade components subjected to cyclic thermal and centrifugal loading, *European Journal of Mechanics-A/Solids* (2022) 104652.
- [24] K.M. Knowles, P.R. Howie, The directional dependence of elastic stiffness and compliance shear coefficients and shear moduli in cubic materials, *J. Elast.* 120 (1) (2015) 87–108.
- [25] M.W. Savage, The influence of crystal orientation on the elastic stresses of a single crystal nickel-based turbine blade, *J. Eng. Gas Turbines Power* 134 (1) (2012).
- [26] X. Zhang, et al., Crystal orientation effect and multi-fidelity optimization of a solid single crystal superalloy turbine blade, *Comput. Mater. Sci.* 149 (2018) 84–90.
- [27] M. Segersäll, D. Leidermark, J.J. Moverare, Influence of crystal orientation on the thermomechanical fatigue behaviour in a single-crystal superalloy, *Mater. Sci. Eng., A* 623 (2015) 68–77.
- [28] N. Hou, et al., The influence of crystal orientations on fatigue life of single crystal cooled turbine blade, *Mater. Sci. Eng., A* 492 (1–2) (2008) 413–418.
- [29] W. He, et al., Film cooling and aerodynamic performances of a turbine nozzle guide vane with trenced cooling holes, *Appl. Therm. Eng.* 150 (2019) 150–163.
- [30] J. Liu, et al., Investigation on cooling effectiveness and aerodynamic loss of a turbine cascade with film cooling, *J. Therm. Sci.* 25 (1) (2016) 50–59.
- [31] J. Wang, et al., The inter-hole interference on creep deformation behavior of nickel-based single crystal specimen with film-cooling holes, *Int. J. Mech. Sci.* 163 (2019) 105090.
- [32] Z. Wen, et al., Prediction method for creep life of thin-wall specimen with film cooling holes in Ni-based single-crystal superalloy, *Int. J. Mech. Sci.* 141 (2018) 276–289.
- [33] Thulin, R.D., D.C. Howe, and I.D. Singer, *Energy efficient engine high-pressure turbine detailed design report*. 1982.
- [34] O. Kauss, et al., Structural analysis of gas turbine blades made of Mo-Si-B under transient thermo-mechanical loads, *Comput. Mater. Sci.* 165 (2019) 129–136.
- [35] S. Wylie, et al., Reduction in flow parameter resulting from volcanic ash deposition in engine representative cooling passages, *J. Turbomach.* 139 (3) (2017).

- [36] Cory, T.M., et al. *Impact of Dust Feed on Capture Efficiency and Deposition Patterns in a Double-Walled Liner*. in *Turbo Expo: Power for Land, Sea, and Air*. 2019. American Society of Mechanical Engineers.
- [37] C.G. Skamniotis, A.C. Cocks, Designing against severe stresses at compound cooling holes of double wall transpiration cooled engine components, *Aerosp. Sci. Technol.* (2021) 106856.
- [38] A. Ma, D. Dye, R. Reed, A model for the creep deformation behaviour of single-crystal superalloy CMSX-4, *Acta Mater.* 56 (8) (2008) 1657–1670.
- [39] R.J. Goldstein, Film cooling, in: *Advances in Heat Transfer*, Elsevier, 1971, pp. 321–379.
- [40] Baldauf, S., A. Schulz, and S. Wittig. *High resolution measurements of local effectiveness by discrete hole film cooling*. in *Turbo Expo: Power for Land, Sea, and Air*. 1999. American Society of Mechanical Engineers.
- [41] J.P. Sellers Jr, *Gaseous film cooling with multiple injection stations*, *AIAA Journal* 1 (9) (1963) 2154–2156.
- [42] Allan, C.D., *Plasticity of nickel base single crystal superalloys*. 1995, Massachusetts Institute of Technology.
- [43] H. Li, M. Wang, R. You, Impact of radiative heat flux on turbine blade heat transfer in high temperature environments, *Appl. Therm. Eng.* 212 (Jul.) (2022) 118505.
- [44] H.H. Cho, D.H. Rhee, Local Heat/Mass Transfer Measurement on the Effusion Plate in Impingement/Effusion Cooling Systems, *J. Turbomach.* 123 (3) (Jul. 2001) 601–608.
- [45] J.H. Lee, S.J. Lee, Turbulent Heat Transfer Characteristics in a Stagnation Region of Axi-Symmetric Jet Impingement, *Proc. 11th IHTC 5* (1998) 433–438.
- [46] A. Andreini, L. Cocchi, B. Facchini, L. Mazzei, A. Picchi, Experimental and numerical investigation on the role of holes arrangement on the heat transfer in impingement/effusion cooling schemes, *Int. J. Heat Mass Transf.* 127 (2018) 645–659.
- [47] B. Coulton, A. V Murray, and P. T. Ireland. A Computational Approach to Aerothermal Analysis of Complex Internal Turbine Cooling Geometries. *Proceedings of ASME Turbo Expo 2022 Turbomachinery Technical Conference and Exposition*. GT2022-81928, 2022.